ZnO-Based nanostructures for gas sensing applications.

POLITECNICO DI TORINO

DEPARTMENT OF APPLIED SCIENCE AND TECHNOLOGY

Doctorate in Electronic Devices

(XXVII ciclo)

# ZnO-based nanostructures for gas sensing applications

**Scientific supervisor:**
Dr. Daniele Pullini

**Advisors:**
Prof. Giancarlo Cicero

Dr. Davide Calestani

Candidate

Athanasios Tamvakos

Marzo 2015

# Abstract

Metal oxide chemical sensors based on nanomaterials are gaining popularity and finding extensive use in automotive industries, process control and environmental monitoring. ZnO, a semiconducting metal oxide has attracted great interest over the years for its sensitivity to a variety of gases. Nanostructured sensing materials, such as thin films, nanowires, tetrapods, nanoflackes offer an inherently high surface area, reducing operating temperatures and increasing sensitivity to low concentrations of analytes. In this thesis, ZnO nanostructures have been tested as chemical sensors and a detailed study on the effect of different process parameters such as grain size, roughness, surface-to-volume ratio, depletion layer, temperature, gas concentration and material properties on gas sensitivity is presented. Initially, ZnO nanodevices were prepared with a variety of techniques, such as RF sputtering, electrodeposition, hydrothermal growth, chemical vapour deposition, thermal evaporation and controlled oxidation. The structural characterization of the nanodevices has been done by a FEI QUANTA 3D dual beam SEM/FIB machine and by a Dimension 3100 Atomic Force Microscope (AFM) (Digital Instruments) in tapping mode. X-ray diffraction (XRD) spectra were recorded on an AXS D8 diffractometer (Bruker) with a Cu Kα X-ray tube. The gas sensor substrate based on alumina consisted of Pt grid of 50nm thickness and golden contacts of 200nm thickness creating an alumina patterned substrate. The sensor deposition area was coated with ZnO nanostructures to form the sensing material. Sensing measurements are performed in a closed steel chamber where air and tested gases have been inserted. ZnO based nanostructures' response was measured in different concentrations of Ethanol, CO and NO2.

Initially the role of grain size and roughness has been investigated in several thin film based nanodevices. Grain size is decreasing with increasing RF sputtering power and increasing by post-annealing treatment. Roughness instead is increasing with both the increasing of RF sputtering power and post-annealing treatment. High response was observed for those films with smaller grain size, while the roughness seems to influence very little the response of the sensor. For all thin films, the response is increasing with

temperature and gas concentration. Recovery time and response time seem to follow a non-linear behavior with the above parameters.

Extended studies have investigated the role of surface-to-volume ratio and depletion layer in the sensing performance. It has been observed that the increase of surface-to volume ratio has an important effect on the sensitivity, increasing, more than twice the response of such a device in respect to another that is based on a ZnO thin film. On the other hand, the dimensions of a nanostructure play the most crucial role in the depletion layer width in respect to the sensing properties. The diameter of a nanowire should be comparable with its depletion layer width. In this case the depletion layer has strong effect, which makes the sensor's response depend also on it.

The sensing properties of all fabricated structures have been compared to find the optimum sensor that could face the demands of automotive industries. All fabricated structures have been compared in different configurations to find out which one presents the best sensing performance. To that direction sensors based on thin film, tetrapods, nanowires, nanoflackes have been tested in same environmental conditions. Advanced nanostructures present better sensing properties. Sensing response of every advanced nanostructure presents more than double sensing response than every thin film-based nanostructure. Comparing the advanced nanostructures with each other, tetrapods based sensor has higher response and recovery time, while the sensitivity is slightly higher for the nanowires-based sensor.

Theoretical studies have been performed by ab-initio simulations in NO2 environment. They have revealed that the sensing mechanism is driven almost exclusively by competitive adsorption between NO2 and atmospheric oxygen mediated by temperature change. The influence of the NO2 on the electronic properties of ZnO has been assessed and it is in accordance with the experiments.

Our future work is the investigation of other materials for the development of sensing nanodevices targeting to develop more sensitive nanosensors in the same or lower cost. Additionally, the investigation of other growth techniques that could develop more complicated structures in low cost is another point of interest for the future.

## Acknowledgement

A thesis is not conceivable without the support of a lot of people. I would like to express my gratefulness to everyone who contributed to this thesis.

First of all I like to thank my cousin and colleague Dr. Dimitrios Tamvakos with whom we lived this great experience together and we had overcame all the obstacles till the end and my supervisor Dr. Daniele Pullini who gave me this great opportunity. It was a pleasure to work in this group. The enthusiasm for new ideas, new collaborations, and also the work I did, always helped me with my dissertation. I appreciated very much the freedom which I could enjoy during the three years of this work.

I am especially grateful to Dr. Luca Belforte and Dr. Nello Li Pira who were my supervisors and consultants in the laboratory and taught me a lot about experimentation and the business of an experimentalist. They also helped me a lot with their precise, very competent and professional advices.

I would also like to express my deep thanks to my external supervisor Dr. Davide Calestani from CNR/IMEM Parma, with whom we were in close collaboration during my research activities; he has disseminated to me the competences that a researcher should have like patience, persistence and ambition. Many thanks also to Professor Giancarlo Cicero from Politecnico di Torino who was my tutor during this period; he was always there to give me advices regarding to the experimental work, modules and presentations; helping me to enhance the related skills. Their expertise in this subject matter has helped me write a very high quality thesis.

How I could forget Dr. Mauro Sgroi with whom I shared the same office for three years. He was always there to give me instant help to whatever I needed. Many thanks also to my other colleagues that passed by my office for short or long period, Dr. Marzia Paderi, Margherita Fioriello and Furio Zadde.

I would also like to thank all the other members of my group; Dr. Vito Lambertini, Dr. Brunetto Martorana, Davide Roncato, Valentina Grasso, Valentina Dellaca, Maria Margherita Dugand, Alessandro Ziggiotti, Dr. Mauro Brignone for their support and the harmonious relationship we have had during my stay at CRF.

Many thanks go to Stefano Zanin, the researcher with whom I have initiated my whole work. I would also like to thank Alina Pruna for giving me experimental instructions and for helping me understand the growth technique of MOS and Dr. Korir Kiptiemoi for our close cooperation in writing scientific articles and exchanging scientific knowledge.

I also want to give my thanks to Irene Cannavaro which was my very first friend at CRF and made me feel comfortable in this work.

Many thanks to the other researchers I had the opportunity to work with the last three years and to become friend with all of them, Elena Verna, Simone Mana, Linda Caringella, Rodrigo Balloni, Bruno Muscato, Alessandra, Ricardo, Sylvia.

I also appreciate and thank colleagues and professors from the Nanowiring network, whose ideas helped me much in the research discussion. Special thanks to Dr. Davide Cammi who helped me understand and develop the CVD technique and grow high quality nanowires.

My hearty thanks go to all of my friends at Turin for doing my daily life very pleasant. Without them it would be impossible to fulfill such a massive work. I am also grateful to all of my friends outside Turin for their support and love and to all of them; family and friends that have paid me a visit during my stay in Turin.

Especially, I am greatly indebted to my mother and sister who were always my firmest support through all of my life. Many thanks also to my father for his support and my small brother; being away for the PhD while he is growing up, I lost some of the very important moments in his life.

“*Who lives sees, but who travels sees more*”

# Table of Contents

## LIST OF FIGURES

## Tables

# Chapter 1 . Introduction

## 1.1 Introduction to gas sensors

The detection of hazardous gases became gradually in the last century an issue of great importance for the industries and for several groups of workers. Environmental threats and accidents that are multiplied by the time have obliged the industries to investing more and more money in the gas sensors development both in research and industrial level.

Starting from many years ago people had realized the importance of the development of sensing devices. For example, miners had used small birds as a substitute for a quantifiable method to measure this hazard. Nowadays there is a huge demand for the development and optimization of detectors for monitoring airborne pollutants, for improvement of the traffic and residential safety, for the protection of workers in the petrochemical and oil industries or even for the detection of natural gas leaks or carbon monoxide from incomplete combustion in boilers in domestic environments. Such kind of devices find numerous of applications also in automotive sector, powertrain manufacturing, transportation industry [1], aerospace industry, optical systems.

A sensor in general could be defined as an electrical or electronic device that detects a signal, physical condition and chemical compounds through a transducer which converts a signal from one form of energy to another [2]. Energy types include (but are not limited to) electrical, mechanical, electromagnetic, chemical, acoustic and thermal energy. While the term transducer commonly implies the use of a sensor/detector, any device which converts energy can be considered a transducer. Some of the most used sensors nowadays are the gas sensors, the thermometer, the thermocouple, the phototransistor, the photoresistor, the microphone, the seismometer, the Hydrophone etc.

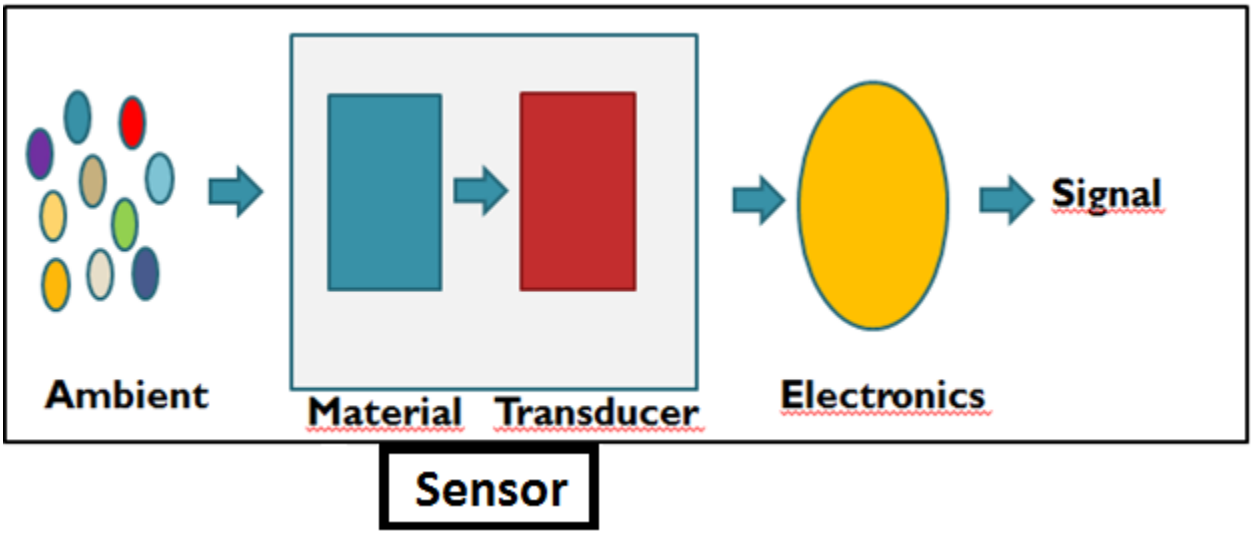


Figure 1.1: Working principle of a high-performance gas sensor.

Gas sensor which is the main topic of the present work is a device that transforms the chemical concentration of one or more specific gases into a signal that can be easily employed to report the detection result [3]. Specifically, gas sensor measures the concentration of gas nearby interacting with a gas to measure its concentration. Each gas has a unique breakdown voltage (i.e. the electric field at which it is ionized). Sensor identifies gases by measuring these voltages. The concentration of the gas can be determined by measuring the current discharge in the device.

## 1.2 Metal oxide semiconductors for gas sensing

Metal oxide sensors are also known as chemiresistors. The detection principle of resistive sensors is based on change of the resistance of a nanostructure upon adsorption of the gas molecules on the surface of a semiconductor. The gas-solid interactions affect the resistance of the nanostructure because of the density of electronic species in it.

Metal oxide semiconductor (MOS) is one of the most important materials that could be applied for gas sensing measurements. It was first discovered in the early 60s that molecules interacting with semiconductor surfaces can influence the surface properties of semiconductors, such as conductivity and surface potential. The first MOS gas

sensors were based on thick films of SnO2 which was reported by Taguchi [4]. Since then, metal oxide semiconductors have been widely studied as gas sensors because of their low cost and relative simplicity. Metal oxides have a broad range of electronic, chemical and physical properties that are often highly sensitive to the changes in their chemical environment. Due to these properties, metal oxides have rapidly gained attention over the years and became the most popular commercial sensors. Nowadays is well known that the sensor characteristics can be changed by varying the crystal structure, dopants, preparation technology, operating temperature etc. Numerous materials have been reported to be usable as metal oxide sensors including both single-component metal oxides such as ZnO, SnO2, WO3, TiO2 and Fe2O3; and multi-component oxides, such as BiFeO2, MgAl2O4, and SrTiO [5].

### 1.3 Material properties of ZnO Semiconductors for gas sensing applications

Zinc Oxide is a wide band gap semiconductor of (~3.3 eV), exhibiting wurtzite crystal structure of hexagonal shape. Its crystal is composed of alternating zinc and oxygen planes, forming the final ZnO structure. In Figure 1.2a the wurtzite crystal structure of ZnO is shown. ZnO's basal plane (0001) is a polar surface, which is terminated at one end by positively charged zinc ions and at the other end by negatively charged oxygen ions. The rest of the crystal surfaces, shown in the left side of Figure 1.2b are non-polar.

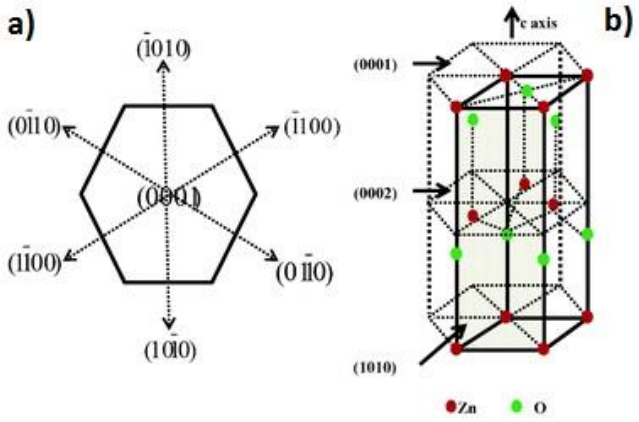


Figure 1.2: Wurtzite crystal structure of ZnO [6].

The technology of modern electronics, as well as the low power consumption need have paved the way of implementing nanostructured materials in the fabrication of novel devices. In the literature a great variety of ZnO nanostructures can be found including nanowires (NW) [7], nanorods (NR) [8], nano-flowers [9] and nanobelts [10]. The discrepancies in the shape of these structures are dictated by the different growth rates along different crystal planes. Addition of catalysts or rate inhibitors during the growth process takes place in order to further control the growth ratio between different crystal planes. In the general case, a crystal forms its structure in such a way as to maximize the surface area of low energy surfaces, as the non-polar surfaces. As presented in Figure 1.2b, the side walls geometry of ZnO (non-polar phases) is maximized, while the polar ends follow a rapid grow at (0001) direction. Consecutively, the nanowire form is the most favored one for ZnO when trying to grow self-assembly nanostructrures.

ZnO has received much attention over the past years for its possible use in wide range of applications such as gas sensors [11] [12] solar cell electrodes [13] [14], light emitting devices [15] and optical waveguide device [16]. The remarkable properties of ZnO include also abundance in nature, low cost, non-toxicity, high chemical stability [17], [18], [19] and amenability to doping. Most of all, the chemical sensitivity to different adsorbed gases make it one of the most widely applied metal oxide material for monitoring of various gases [20], [21], [22].

In particular, ZnO nanostructures have been identified as a promising candidate for gas sensing due to their excellent response and recovery characteristics to a variety of analytes such as NO2, NO, CO, CO2, ethanol, methanol etc.

## 1.4 Motivation and objectives

Researchers in the past have reported improvement in sensitivity for gas sensors by using nanostructured materials [23], [24]. However less work has been reported on the comparison between different nanostructures and different fabrication methods in terms of sensing properties. The motivation of this work was to fabricate highly sensitive gas sensors operating at low temperatures by using several deposition methods in order to propose the optimum development way and the optimum nanostructure to the scientific community for gases detection use.

To this direction the potential use of ZnO seed layers with different grain size and thickness capable to host nano-objects has been investigated. We would like to report on grain-size effect approach towards improving the sensing properties of ZnO thin films deposited by RF sputtering at low gas concentration levels. The morphological and structural properties of the films were analyzed as a function of sputtering power at room temperature and subsequent annealing treatment while the gas sensing ones were studied in low gas concentration range under low operating temperature. The obtained results indicate the high potential of grain-size effect as an approach to the development of high-sensitivity ZnO-based sensors.

We would also like to open the way to low cost but high performing gas sensors by comparing the ZnO-based seed layers with sensors made by either ZnO-based nanostructures or by hosting nano-objects on top of the seed layers in sensing properties such as sensitivity, response, response and recovery time, reversibility and reproducibility. As nano-objects have been used nanostructures such as thin film, tetrapods, nanowires and nanoflackes which have been fabricated by several methods such as electrodeposition, chemical vapor deposition, hydrothermal growth, RF sputtering,etc.

# Chapter 2 . Investigation of the sensing characteristics and dangerous gases detection

## 2.1 Sensing properties

Characterizing sensor's performance requires taking into account several parameters [25]. Below are listed the most important parameters followed by their definitions:

### Response

As sensor response is defined the relative percentage variation in the sensor conductivity [26], and is given by using the formulas below

$$\text{Response} = (G_{gas}-G_{air})/G_{air}, \text{ in case of reducing gases}$$

Where $G_{gas}$ is the conductance of the sensor when is exposed to the gas and $G_{air}$ the base conductance of the sensor when is exposed only to air without reducing gas.

$$\text{And, Response} = (R_{gas}-R_{air})/R_{air}, \text{ in case of oxidizing gases}$$

Where $R_{gas}$ is the Electrical resistance of the sensor when exposed to the gas and $R_{air}$ is the electrical resistance of the sensor when exposed only to air without oxidizing gas.

### Sensitivity

Is the change in the measurement signal per concentration unit of the analyte, i.e. the slope of a calibration graph, namely the derivative of response. In other terms is the response change (ΔR) of a sensor divided by the related variation of the input gas concentration (ΔC) as described appears at the equation below:

$$\text{Sensitivity (\%/ppm)} = \Delta R/\Delta C$$

## Response and Recovery Time

Response time is defined as the rise time (time interval) that the output response of a sensor goes through from 0% to 90% of the final steady-state value upon reached stationary conditions. While recovery time is defined the fall time that the output response of a sensor goes through from 100% to 10% of the final stready-state value upon reached stationary conditions. Two examples follow:

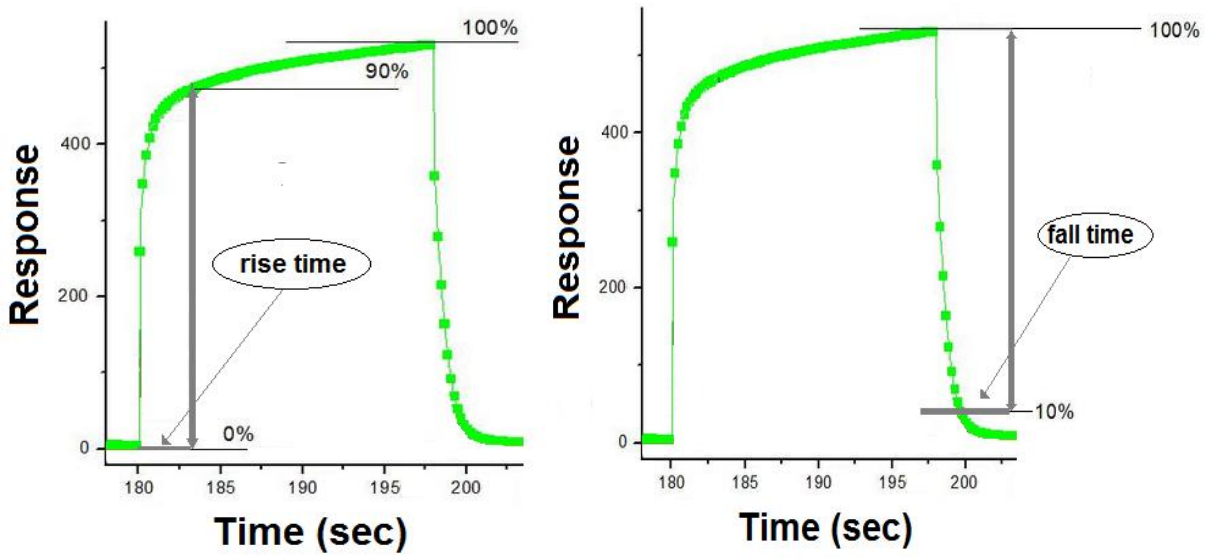


Figure 2.1: Response time and Recovery time of a random sensor.

## Reproducibility

Is the degree of agreement among results of successive measurements of the same measurand when individual measurements are preformed changing the following conditions.

## Limit of detection

In metrology and analytical chemistry, the limit of detection (LOD) is defined as the minimum gas concentration (measurand) detected by a sensor (instrument).

## Dynamic (or operation) range

Is the concentration range between the detection limit and the upper limit concentration.

## Selectivity

An expression of whether a sensor responds selectively to a single analyte or a group of analytes (quantitative expressions of selectivity exist for different type of sensors). An example of ideal case and one of real case follow:

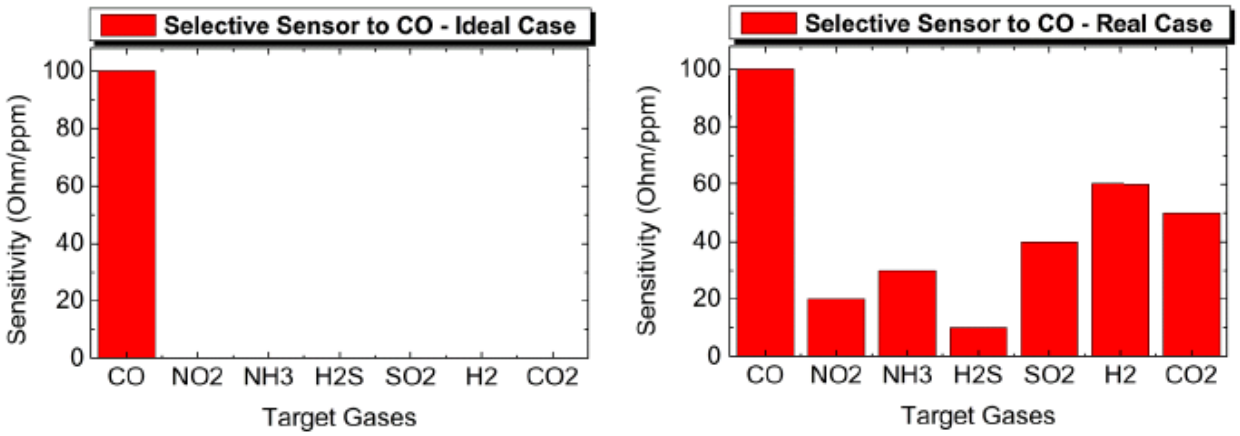


Figure 2.2: Sensors selectivity to CO a) Ideal case b) Real case.

## Linearity

Is the relative deviation of an experimentally determined calibration graph from an ideal straight line. Usually values for linearity are specified for a definite concentration range.

## Resolution and noise

Is the lowest concentration difference that can be distinguished when the composition is varied continuously. This parameter is mainly important for sensors in continuously

flowing streams. Resolution, in principle, is limited by the noise occurring both on the sensor (active material) and electronics (amplifier) used to readout the sensor response.

## Hysteresis

Is the maximum difference in output when the value is approached with an increasing and a decreasing analyte concentration range. It is given as a percentage of full scale output.

## Stability

Is the ability of the sensor to maintain its performance for a certain period of time. As a measure of stability, drift values are used (e.g. the signal variation for zero concentration).

## Working Temperature

Is usually the temperature that corresponds to maximum sensitivity.

## Accuracy

The given definition is the attitude of a sensor to give an indication close to the true value of the measurand under test. The concept is clarified in Figure 2.3.

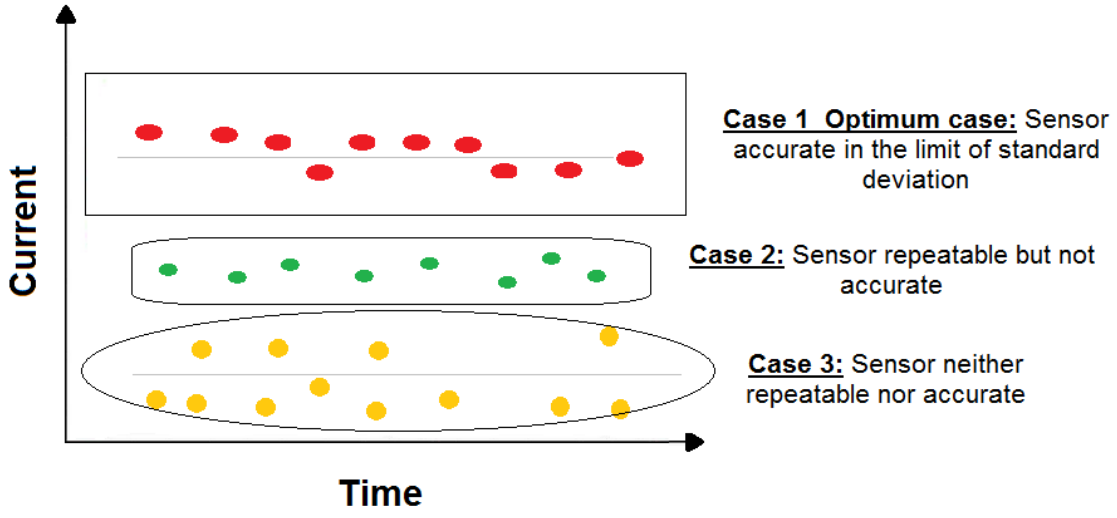


Figure 2.3: Cases that may correspond to the attitude of the sensor.

## 2.2 Classification of gases using gas sensor models

There are two categories of gases:

1. Oxidizing gases or electron-accepting gases, such as $NO_2$, $O_2$, $O_3$ etc.
2. Reducing gases or electron-donating gases, such as Ethanol, CO, $NH_3$, $H_2$, $H_2S$, $SO_2$, $CH_4$, $CO_2$ etc.

In case of n-type semiconductor (when a semiconductor contains mostly free electrons it is known as "n-type") and in particular in case of ZnO sensing material (n-type as well) the sensing procedure for both gas types is presented in schemas below (Figure 2.4 and Figure 2.5).

Reducing gases induce a decrease in the electrical resistance of ZnO-based sensor (n-type). Oxygen molecules remove from materials surface the gas molecules, thus electrons which were previous captured return to valance band leading in the increase of conductivity.

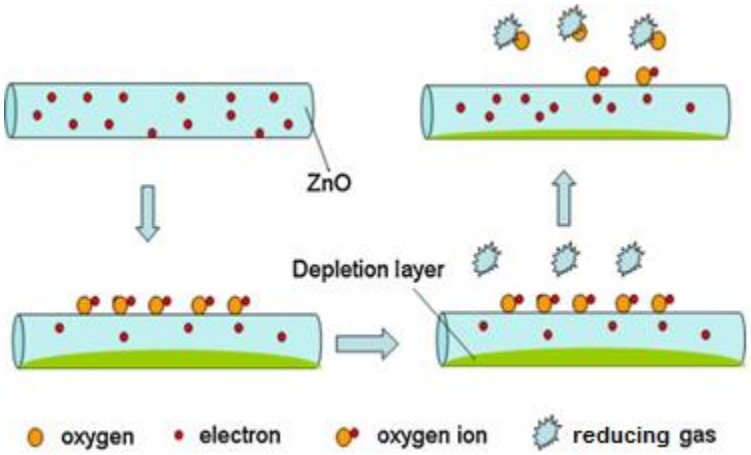


Figure 2.4: Nanowire model of conduction mechanism upon exposure to reducing gas.

On the other hand oxidizing gases induce an increase in the electrical resistance of ZnO-based sensor (n-type). Oxygen molecules adsorbed by the material surface act as electron acceptors. The adsorbed oxygen species capture free electrons from Zn metal giving rise to an increase of resistance.

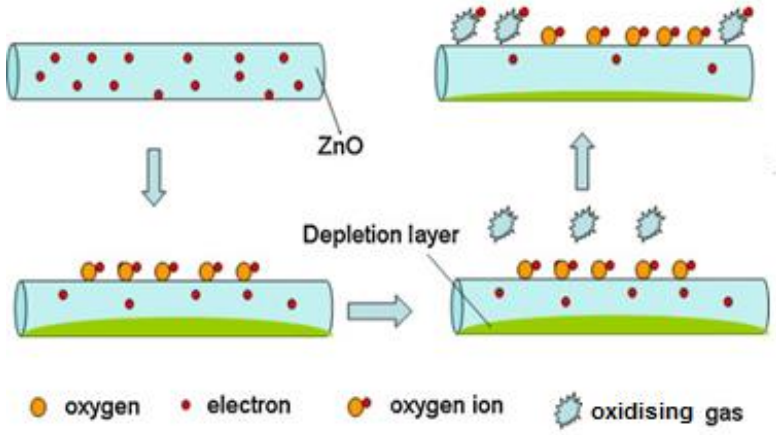


Figure 2.5: Nanowire model of conduction mechanism upon exposure to oxidizing gas.

Band models of conductive mechanism upon exposure to both oxidizing and reducing gases are given in next chapter for better understanding of the fundamental mechanisms that cause the gas response at MOS.

## 2.3 Detection of Gases

In this section the details of the gases of major interest for the automakers are reported. In literature there are several of those gases that referred as highly toxic, toxic or dangerous. The detection of those gases is a challenging issue and the details of each one of them must be known.

### 2.3.1 Detection of Nitrogen oxides

Nitrogen oxide gases, commonly referred to collectively as NOx, are common pollutants formed in automotive engines and industrial combustion systems by thermal fixation and oxidation of atmospheric nitrogen. NOx, which includes NO2 and NO gases have adverse effects on the environment, and are the leading cause of green house effect, acid rain, and photochemical smog. In humans, exposure to more than 3 ppm of NO2 gas for period longer than 8 hours can cause respiratory and cardiovascular diseases. Thus, better detection of such gases is of major importance, and that calls for better understanding of detection mechanism to facilitate development and optimization of sensing devices.

### 2.3.2 Detection of Alcohols

Sensor materials for detection of alcohols, especially ethanol, are being actively developed [27]. The interest in ethanol is connected with its wide application in chemistry, medicine, and the food industry and several potential applications such as in case of automakers for traffic safety. Precise quantitative detection of ethanol vapors is required for determination of quality of wines and human health as well. Metal oxides are widely used for detection of ethanol. Ethanol sensors are being enhanced, and as is the case for other analytes, the problems of response, sensitivity, selectivity, stability and reproducibility are being addressed. The most widely used metal oxide materials for alcohol detection are ZnO, TiO2, SiO3, WO3, SnO2 and Zr2O3. As a rule, the analysis is carried out at temperatures above 400°C; therefore one important task is to decrease the operating temperature.

### 2.3.3 Detection of Carbon oxides

CO is a substance produced from the combustion (burning) of carbon based substances. Development of gas sensors for the detection of carbon monoxide is an issue of the day, since CO is one of the most toxic gases, and being odorless, it can form undetected by incomplete combustion of fuel in industry and in private houses. CO gas, which is contained in automobile exhaust along with nitrogen oxides, is one of the main environmental contaminants, especially in large cities. Another carbon oxide, $CO_2$, is one of the greenhouse gases, which are believed to be responsible for the global warming effect. The main source of $CO_2$ today is the combustion of fossil fuels. The number of papers devoted to development of new CO sensor materials is rather small. Some recently developed sensor materials for CO and $CO_2$ are SnO2/TiO2: Nb [28], ZnO [29] [30] , ZnO:Cu [31] and SnO2/Au [32]. The need of improve ZnO-based sensors in the detection of CO is still a high challenge for the scientific community.

Sensor response is suggested to be based on the CO oxidation reaction:

$2CO + O_2 = 2CO_2 + e$ [33]

# Chapter 3 . Synthesis and characterization of ZnO-based nanostructures gas sensors.

## 3.1 Host-device

The substrates used to host the sensing material consisted of an alumina patterned substrate of 3x3 $mm^2$ dimensions. They were patterned by Au contacts (50 nm thick film) and Pt heating elements (200 nm thick) with the sensor geometry map depicted in Figure 3.2 using RF sputtering process (details of RF sputtering procedure reported below in this chapter). The deposition area presented in Figure 3.2 in our experiments hosts the sensing material in all cases. Different shadow masks were used for the deposition of Pt and Au contacts (Figure 3.1). The thickness of Au film was negligible since it was needed just to be conductive with good adhesion and in case of 50nm the two conditions are fulfilled. Pt film created was around 200nm thick. It was noticed experimentally that this was the optimum thickness to create a resistance of 5 Ohm between the two edges of the Pt grid. In this case was easier to heat up the sensor in the desired operating temperature without damaging it.

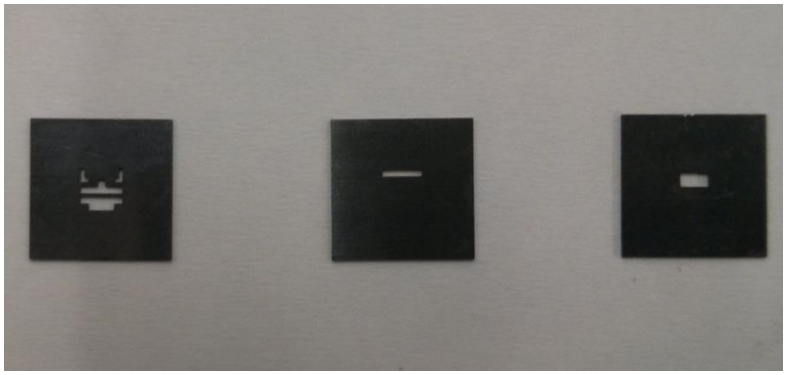

Figure 3.1: Shadow masks for the deposition of Au, Pt and sensing material (from left to right).

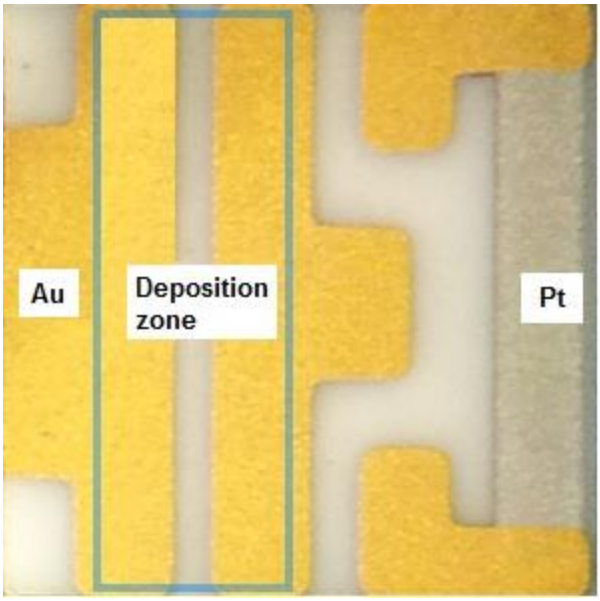


Figure 3.2: Alumina patterned substrate used as host device.

## 3.2. RF sputtering method

Sputtering is a physical process whereby atoms in a solid target material are ejected into the gas phase due to bombardment of the material by energetic ions (Figure 3.3). It is commonly used for thin-film deposition and functional coatings as well as integrated circuit processing [34]. The coating is a multilayer containing silver and metal oxides such as zinc oxide, tin oxide, or titanium dioxide. Sputtering is also used as the process to deposit the metal layer during the fabrication of CDs and DVDs.

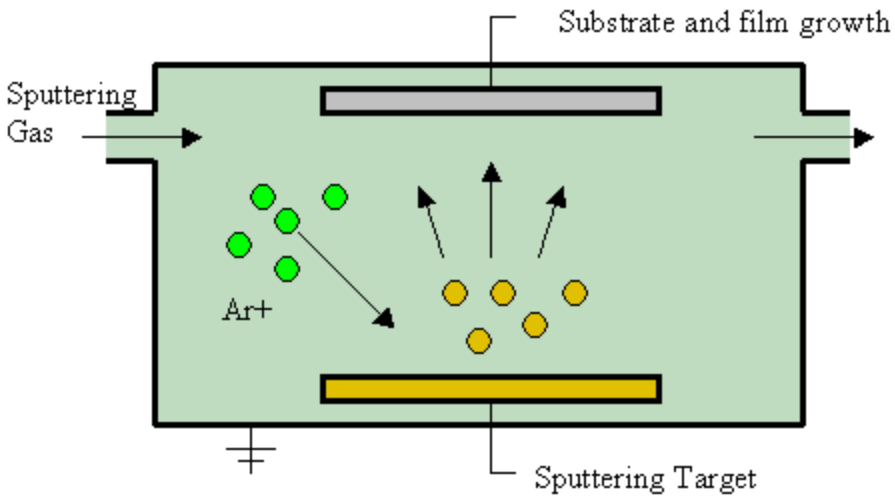


Figure 3.3: RF sputtering deposition procedure.

In general, two stages are distinguished in thin film growth; initial growth which can be separated between nucleation and coalescence and actual growth. During initial growth, chemical and physical properties of the substrate, and interaction between substrate and particles arriving there, play an important role. After an initial layer covering of the substrate has formed, actual growth begins, during which interaction only occurs between particles of the film material. Important parameters are the energy of the particles arriving at the substrate film surface, energy absorption at the time of collision, and chemical and physical interaction between adatoms and the substrate-film surface as well as temperature. These parameters determine the shape, the geometry and the texture of the film [35]. Sputtered ZnO films are polycrystalline, and their individual crystals grow in different orientations, preferentially along their c-axis.

Additionally, in literature can be found growth models for metal oxides thin films formations [36], [37]. The most well known of these models [38] devides the film growth in four different zones. The temperature and the pressure are the parameters that influence the quality of the film and are presented in xx' and yy' axis respectively in Figure 3.4. Zone 1 allows the formation of rough surfaces due to low adatom mobility (slow surface diffusion) and the "shadow effect". Passing to zone 2 the adatom mobility increases, and finally overcomes the shadow effect in order to grow dense layers with

more columnar grains. Finally, in zone 3 small grains coalescence to form larger, not necessarily columnar. The last zone is called T zone, where grain outlines are difficult to identify. ZnO sputtering procedure can be described by the previous model as well.

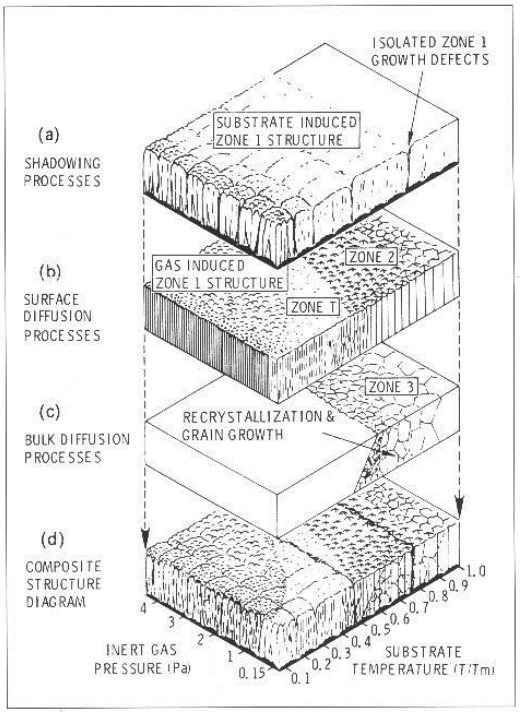


Figure 3.4: Structure Zone Model combining the effect of inert gas pressure and substrate temperature [38].

### 3.2.1 RF sputtering deposition of thin films

The ZnO films were prepared by RF sputtering in the sputtering geometry as shown in Figure 3.5. The sputtering target used was a 2 inch. diameter ZnO target (99.99% purity, 2" diameter x. 250" thickness) which was set at 9 cm apart from alumina patterned substrate. High purity Ar gas was introduced in the chamber set at a vacuum of $2x10^{-6}$ Torr. The deposition was performed by varying the sputtering power from 70W to 150W range from 18 to 75 min in order to obtain film thickness of 100 nm and 200 nm. Further annealing treatment was performed to chosen samples to investigate the grain size and roughness alternation and the structural deformation. Thermal annealing was applied in inert environment for 60 min at 400°C (MILA-5000).

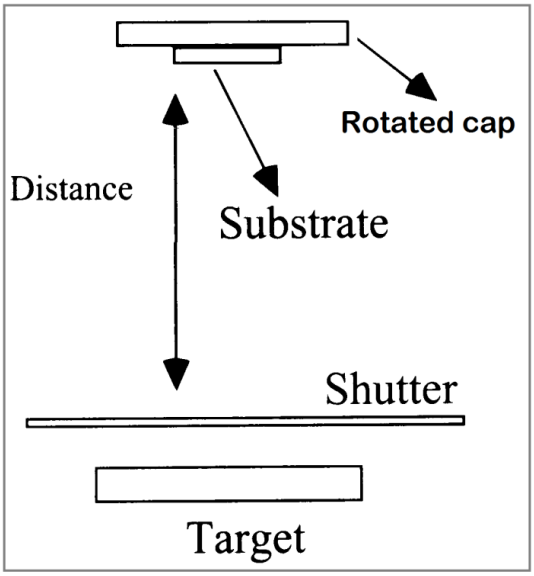


Figure 3.5: RF sputtering geometry inside the chamber.

### 3.2.2 Characterization

Thin films were obtained and characterized mainly by Atomic Force Microscope measurements (AFM) and X-Ray diffraction (XRD) analysis. SEM measurements have been carried out as well but were unable to give sufficient information about the surface structure. The XRD patterns depicted in Figure 3.6 coming from 200nm thin films sputtered at 70 W in the first case (left) and 150 W sputtering power (right) in the second case. The growth rate was 4.15 and 7.96 nm/min respectively. The morphological analysis indicated the presence of all known theoretical peaks for ZnO material, in both cases. No preferential growth was observed during the thin film synthesis and a polycrystalline material was formed.

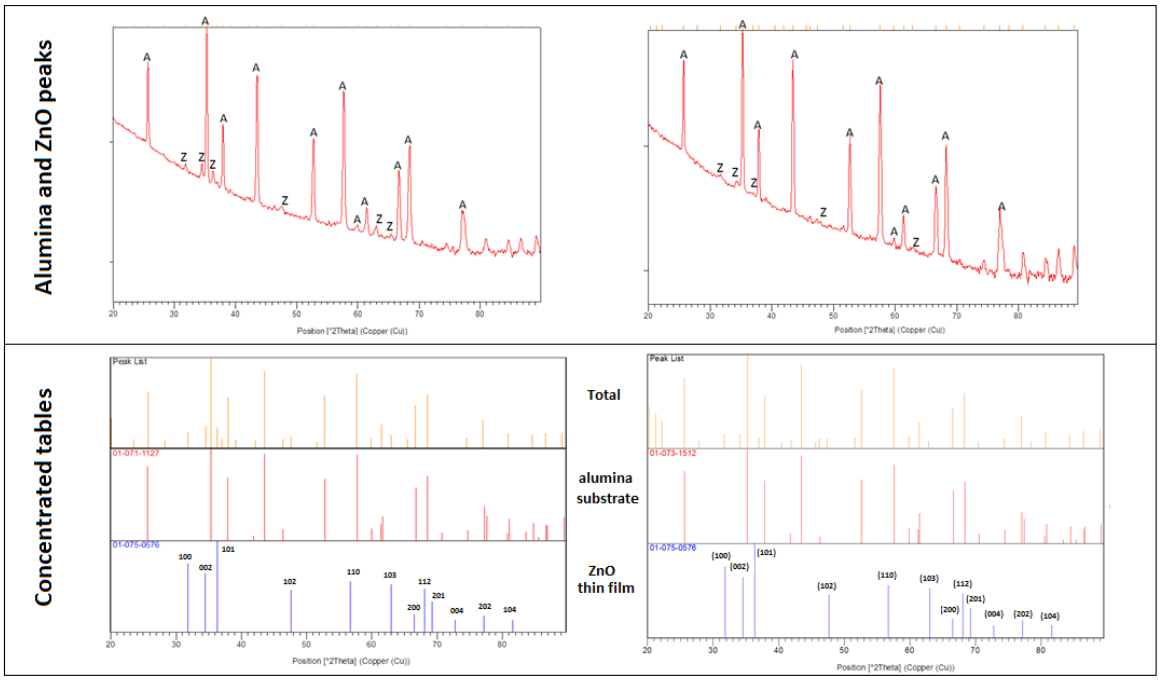


Figure 3.6: XRD and peak analysis of a 200 nm thickness ZnO thin film by RF sputtering at 70 W and 150W (from left to right).

### *3.2.2.1 Annealing treatment*

Moreover, the effect of the annealing treatment on the grain size was analyzed by AFM measurements. Figure 3.7 and Figure 3.8 depict the morphology of 200 nm thick films of ZnO deposited at 70W and 150 W respectively, before and after the annealing procedure. As presented clearly, annealing treatment results in an increase of the grain size in agreement with other previous reports [39]. Roughness is found to increasing with both increasing sputtering power and annealing (Table 1). Numeric details on roughness are given in results and discussion chapter.

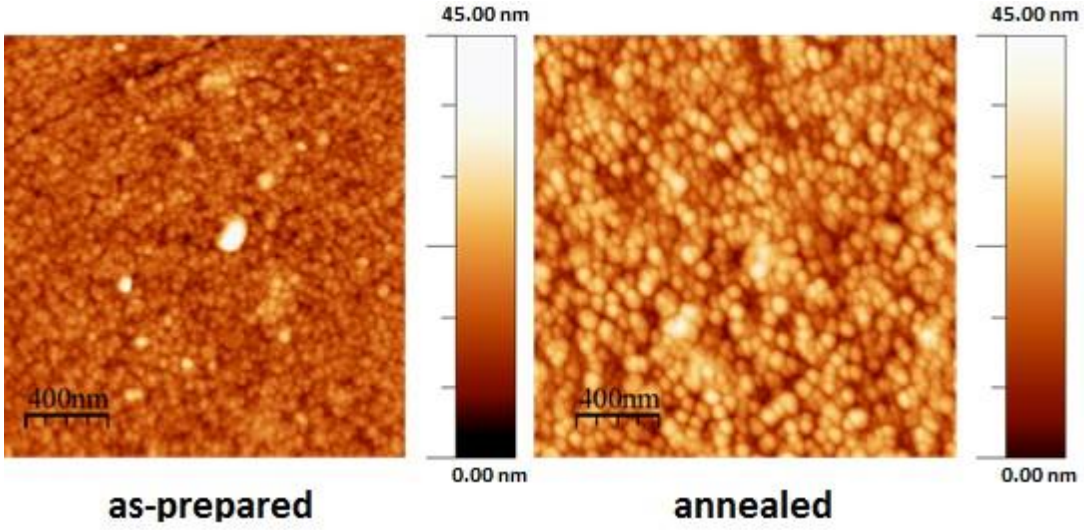


Figure 3.7: AFM images of ZnO film were deposited at 70W before (left) and after annealing (right).

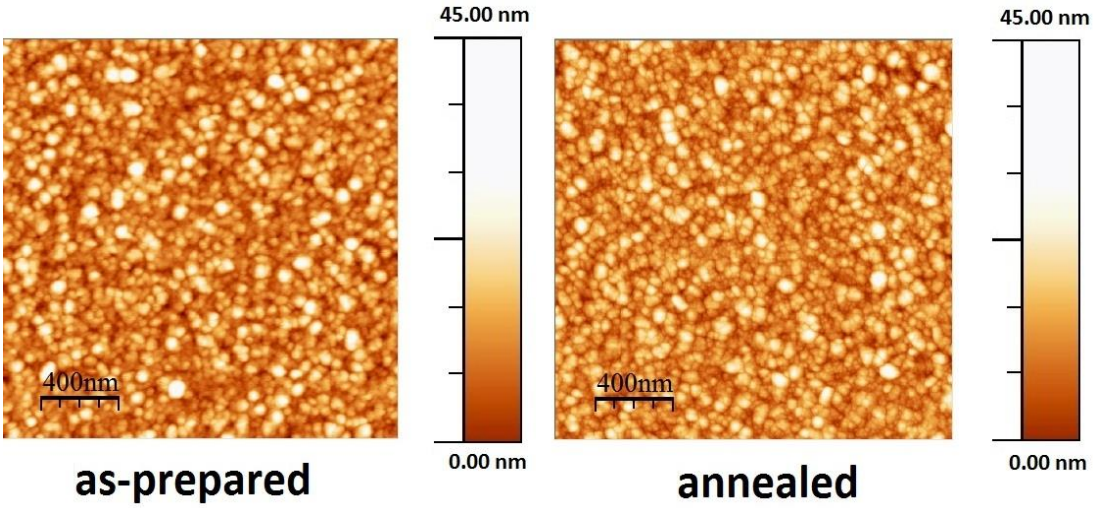


Figure 3.8: AFM images of ZnO film were deposited at 150W before (left) and after annealing (right).

| | ***Increasing sputtering power*** | ***Annealing*** |
|---|---|---|
| ***RMS Roughness*** | increases | Increases |

Table 1: Thin films' roughness in respect to the increasing temperature and annealing.

## 3.3 Electrodeposition method

The electrodeposition method is one of the most widely used methods to synthesize metal oxide nanostructures. Although the electrodeposition method can be used on an industrial scale, all of our work was performed at laboratory scale. ZnO nanowires were synthesized by three different configurations which are analyzed in this chapter.

For electrodeposition, a standard three-electrode setup (Figure 3.9) is typically used, with a saturated Ag/AgCl electrode as the reference electrode and Pt as the counter-electrode. The anode, where growth usually takes place, is placed parallel to the cathode in the deposition solution. The electrical bias throughout the reaction system is controlled by a constant voltage source to maintain a constant driving force to the reaction, or by a constant current source to keep a constant reaction rate.

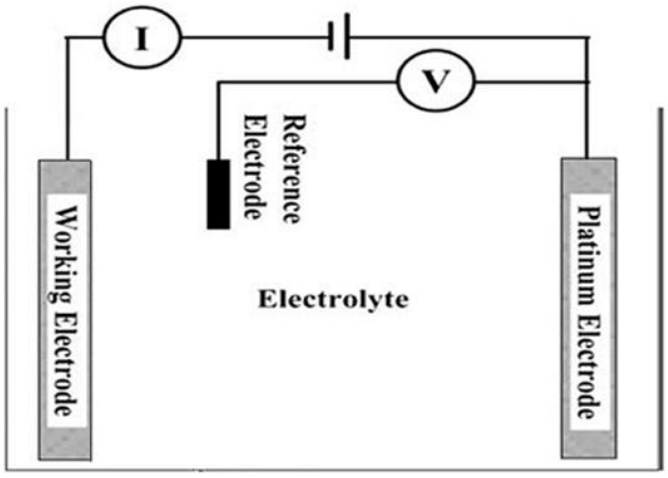


Figure 3.9: Three electrode set-up geometry.

The device was used for the current generation is presented in Figure 3.10. It is an AMEL System 5000 potentiostat-galvanostat.


Figure 3.10: AMEL System 5000 potentiostat-galvanostat.

Zinc and Oxygen ions are provided from the following solution: 5mMol ZnCl2, 0.1M KCl, 5mMol $H_2O_2$ at 75°C which constitute the electrochemical bath. ZnO electrodeposition consists in generating hydroxide ions at the electrode surface by cathodically reducing an oxygen precursor ($H_2O_2$). The chemical equations and reactions [40] are presented in Table 2 and Figure 3.11 respectively.

In details, it was noted that the increase of nanowire length with electrical charge (i.e. time) follows an exponential law at a given over potential. An explanation for this trend could be as follows: during the growth period of the nanowires, the precursor could continuously provide liberally reactants for electrodeposition by ion diffusion and the variation of $HO^-$ and $Zn2^+$ concentrations could be negligible at the substrate surface in a certain period up to the necessary time. Above this period of time, the solution facing the WE surface depletes from ions and so, the precursor could not supply adequate reactants for the growth of nanowires. A boundary layer is formed near the membrane surface (Figure 3.11b). In this region, transport phenomena supply the electrode with ions coming from the solution and a diffusion controlled limiting current density would be obtained [41][42]. In general, the boundary layer reduces the effectiveness of the entire process due to the area of oriented H2O molecules formed in front of the cathode.

Therefore, the crucial steps become the diffusion process of ions and electrochemical reduction of H2O2, which will result in the decrease of the growth rate.

**Hydrogenperoxide : $H2O2 + 2e^- \rightarrow 2OH^-$**

**Molecularoxygen: $O2 + 2H2O + 4e^- \rightarrow 4OH^-$**

**Dehydration: $Zn(OH)2 \rightarrow ZnO + H2O$**

Table 2: Reactions at the cathode surface.

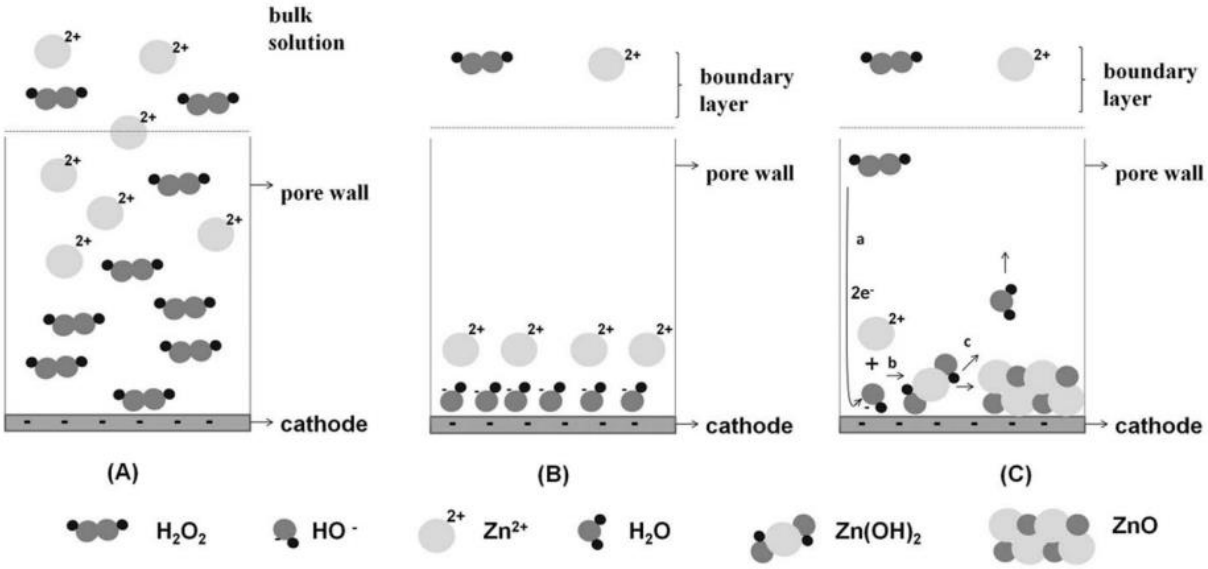


Figure 3.11: Schematic of the electrodeposition of ZnO from ZnCl2 solution with H2O2 as oxygen precursor (adapted from [40]).

ZnO nanowires can be grown by electrodeposition methods in combination with templates, such as anodic aluminum oxide (AAO), polycarbonate membranes, nano-channel glass, and porous films. In the literature, polycarbonate and AAO have attracted much of interest due to their simplicity and capability of large area fabrication [43]. After nanowire growth, the template can be chemically dissolved and leaving behind the free standing nanowires.

### 3.3.1 Electrochemical deposition free standing ZnO nanowires

Initial experiments were performed in pre-deposited ITO glass (Indium tin oxide coaters) in order to investigate the deposition growth parameters. The electrolyte prepared was a solution containing 5 mM of ZnCl2, 0.1 M of KCl and 5 mM of H2O2. The presence of zinc chloride and hydrogen peroxide was explained previously. The addition of potassium chloride in the solution guarantees the good electrical conductivity of the electrolyte. All experiments were controlled via the AMEL 5000 Potentiostat/Galvanostat (presented previously).

Before the actual deposition linear polarization studies were performed on ITO covered glass as reported (Figure 3.12). The method consists in generating hydroxide ions at the surface of the cathode by reduction of the oxygen precursor. The cathodical reduction was observed from -0.75 V to -1.1 V, meaning that any used potential value within this range is capable of initiating the deposition of ZnO nano-structures.

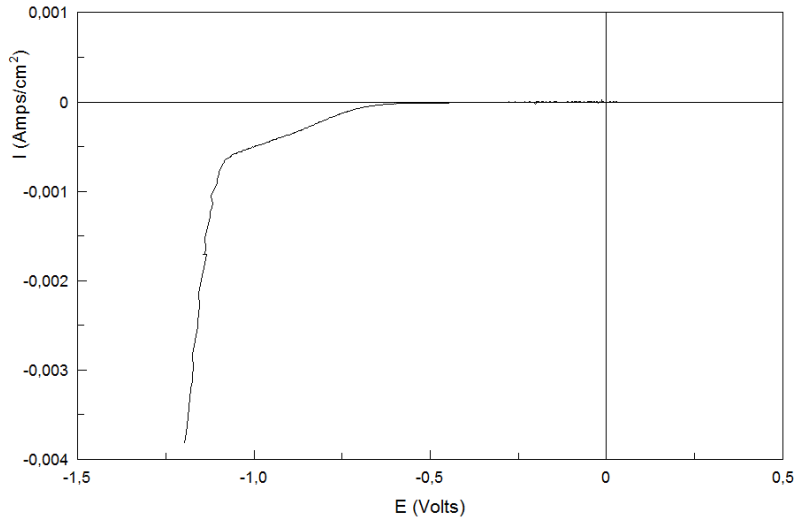


Figure 3.12: Voltammetric curve of ITO covered glass in 5 mM of $ZnCl_2$, 0.1 M of KCl and 5 mM of $H_2O_2$ at a scan rate of 100 mV/sec.

Therefore, the potential values in the range -0.75 V to -1.1 V were applied, following the potentiostatic mode (or chrono-amperometric mode) and the effect of deposition potential on the obtained ZnO nanowires was assessed. It is noted that the length of nanowires depends on the deposition time while the diameter on the applied potential and KCl concentration. In our experiments the KCl concentration was from 0.05 M to 0.1M for the investigation of the optimum growth parameters.

#### *3.3.1.1 Characterization*

Several nanowires were obtained using this configuration. Their diameter and length vary depending on the concentration of KCl and deposition as was mentioned previously. The higher the KCl concentration the bigger the diameter is (Figure 3.13) and the longer the deposition time the higher the length is. Additionally, higher Zn concentration in nanowires synthesis was observed when the deposition potential is decreasing. Finally, the density of the nanowires depends on the applied voltage as presented in Figure 3.14. In Figure 3.15 an image of grown nanowires on SnO2 coming from literature is presented for comparison reasons.

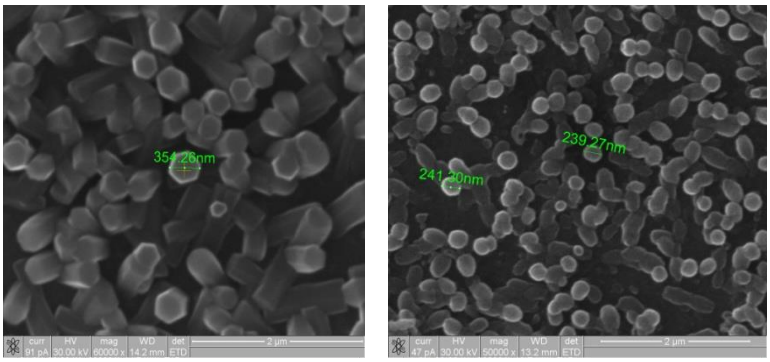


Figure 3.13: SEM image of free-standing ZnO nanowires grown by different KCl concentrations at -800mV.

a)(ZnCl2: 5mM, KCl: 0.1M, H2O2: 5mM)

b)(ZnCl2: 5mM, KCl: 0.05M, H2O2: 5mM)

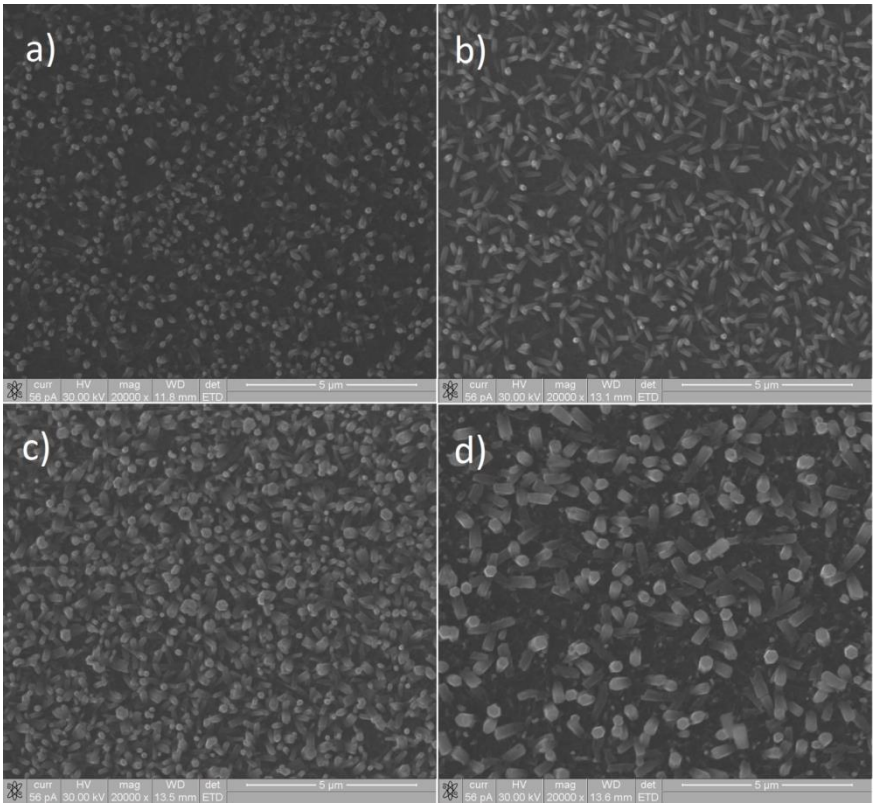


Figure 3.14: SEM micrographs of electrodeposited ZnO nanorods on ITO substrates by potentiostatic mode, (a) -700 mV, (b) -800 mV, (c) -900 mV and (d) -1000 mV.

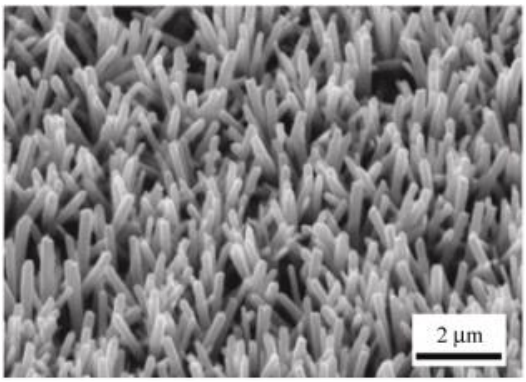


Figure 3.15: SEM image of free-standing ZnO nanowires formed on a SnO2 substrate by electrodeposition (adapted by [44]).

A typical I-t diagram of ZnO deposition in a conductive (ITO) surface is presented in Figure 3.16 shows that the resistance is decreasing during the deposition which is expected since the surface is covered gradually by a less conductive material.

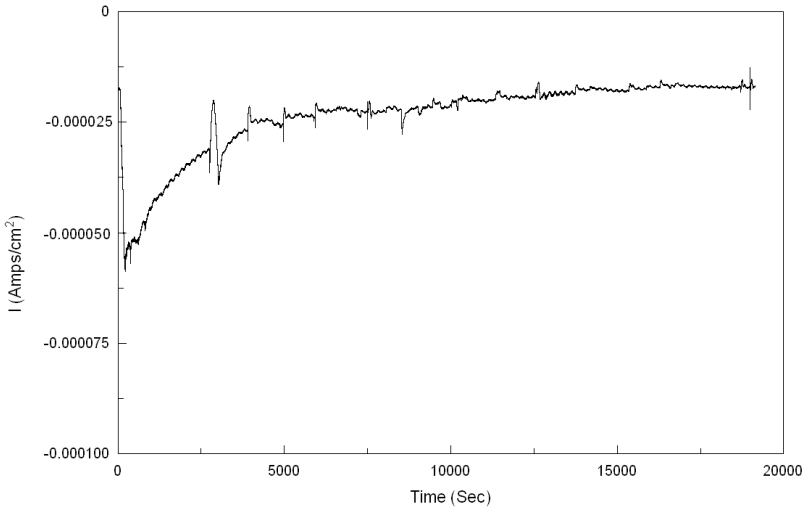


Figure 3.16: I-t diagram of ZnO deposition on ITO surface.

### 3.3.2 Electrochemical deposition of ZnO nanowires in anodic porous alumina template

For the fabrication of the APA template a complicated and lengthy process has followed (Figure 3.17). Using an ITO substrate a titanium thin film which serves as adhesion layer is deposited by thermal evaporation. Titanium film deposition is followed by the deposition of a thicker film of tungsten (using the same method) which serves as adhesion promoter; and on the top via RF sputtering technique first and electron beam evaporation secondly a thick film of around 500nm of aluminum is deposited.

The two step anodization process was followed for the fabrication of APA. The first step was made using oxalic acid for several minutes, which is followed by the etching of APA using CrO3 in order to lead the second anodization directly to the fabricated holes. Using once again the oxalic acid the second anodization had been performed and it was followed by the widening in order to remove tungsten and titanium and to create the contact with the ITO surface. The fabricated APA in its final form is presented in Figure 3.18 at top view along with a SEM image.

The procedure at the end is followed by electrodeposition to grow the vertical aligned nanowires. At the end APA can be chemically dissolved in order to release the free standing nanowires.

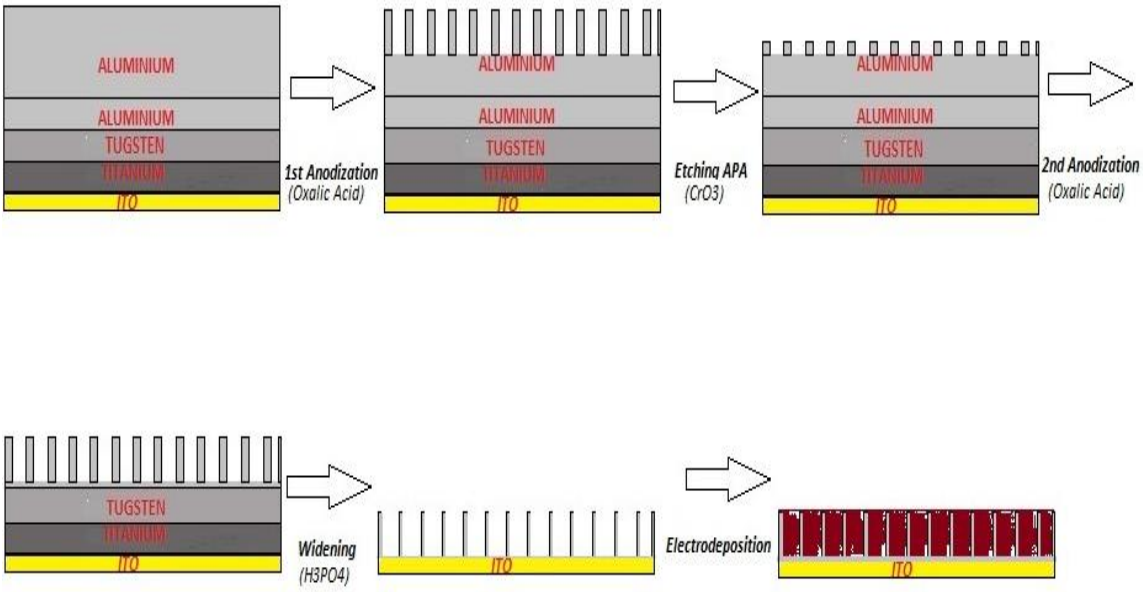


Figure 3.17: Fabrication process steps of home-made anodic porous alumina.

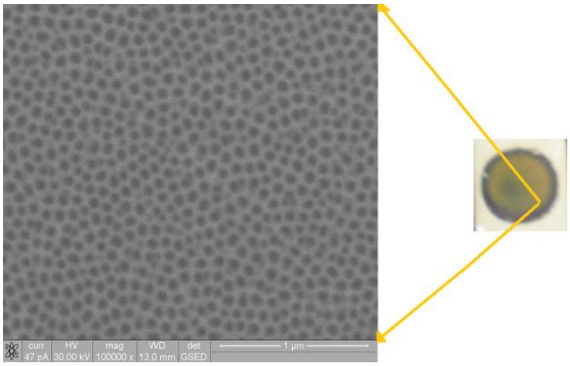

Figure 3.18: APA template (SEM and optical image).

### *3.3.2.1 Characterization*

SEM measurements have been carried out to investigate the nanowires structure. According to the obtained images the density of nanowires was rather poor and in some cases some broken or not well-formed nanowires were also observed. Furthermore, in several templates uncovered holes were noticed. Further investigation is ongoing for the improvement of this technique. EDAX analysis has been performed revealed the presence of Al coming from the dissolved APA, Zn and Au coming from metallization of the sample (Figure 3.20).

SEM images in Figure 3.19 coming from literature [44] present ZnO Nanorods electrodeposited into thin alumina template by potentiostatic method.

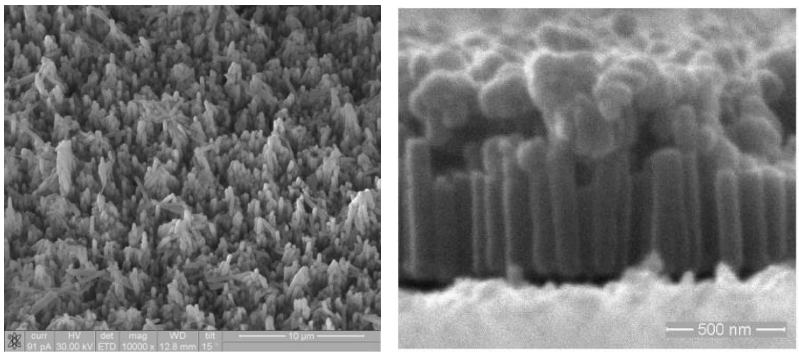


Figure 3.19: SEM images of the ZnO nanorods electrodeposited into thin alumina template by potentiostatic method in 0.1 M Zn(NO3)2 in DMSO (adapted by [45]).

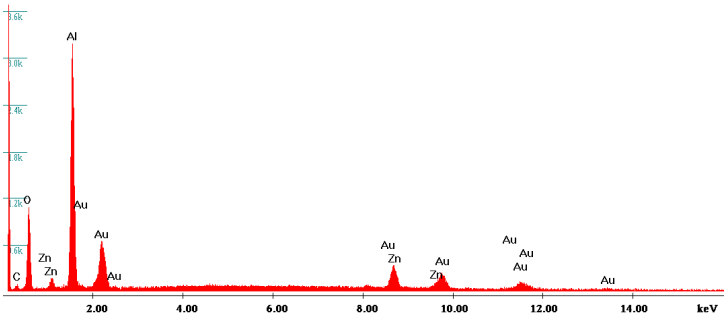


Figure 3.20: EDAX analysis of ZnO nanowires obtained after the dissolution of APA.

### 3.3.3 Electrochemical deposition of ZnO nanowires in polycarbonate template

Commercial polycarbonate membranes with holes created by ion bombardment were used for the deposition. Several templates were used with holes diameter and length varying from 10 to 100 nm and from 5 to 16 um respectively. The thermal evaporation technique was used to create a bottom contact and to cover the holes on the one side. The chosen material for this purpose was Au because it has better adhesion and does not damage the polycarbonate membrane.

The working electrode in this case immersed into the electrolyte by a pipe system made by Teflon (Figure 3.21). The pipe has an aluminum component inside it which is used to contact the polycarbonate membrane isolating the Au covered side and exposing the side with the open holes to the electrolyte.

The fabrication and deposition procedure is presented schematically in Figure 3.22.

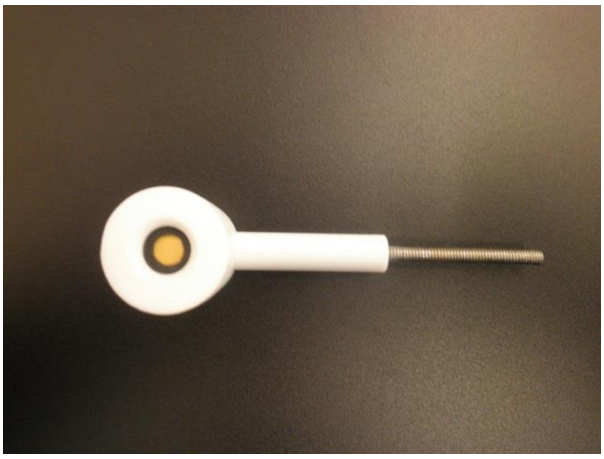

Figure 3.21: The pipe system used for the isolation of one side of polycarbonate membrane from the electrolyte.

In ideal case, the deposition is taking place until the fully cover of the holes. Experimental finding revealed that is rather impossible to achieve a simultaneous and homogenous fill, therefore the deposition in our experiments stops when we observe

that in I-t deposition curve the current starts to decrease, which means that instantaneously the resistance has stopped to increase and therefore the holes are fully covered and the deposition of a thin film (responsible for the resistance decrease) on top of polycarbonate membrane has initiated to be formed (Figure 3.22). After the end of the deposition the polycarbonate membrane can chemically dissolved releasing the nanowires into a suspension of isopropanol. Ultrasonic is used to eliminate the precipitation.

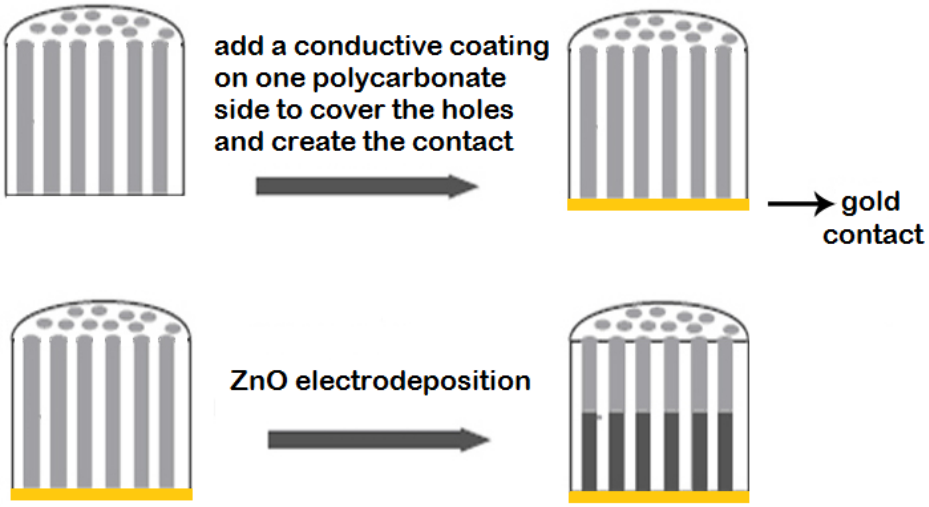


Figure 3.22: Schematically presentation of the steps of TED process.

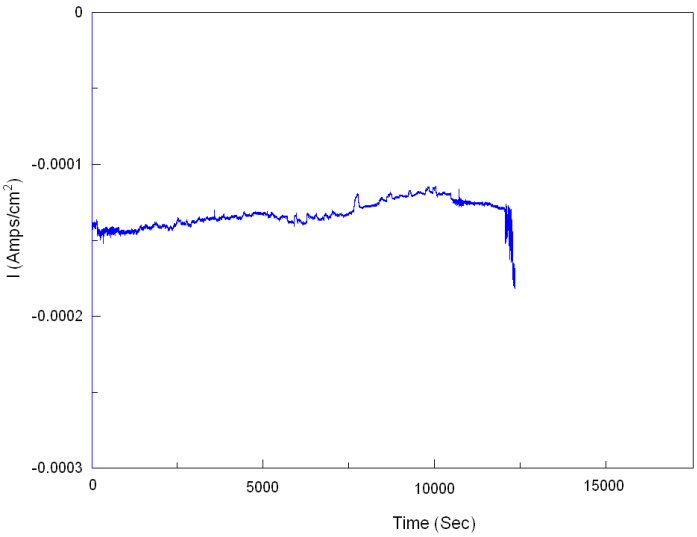


Figure 3.23: I-t diagram presents the deposition into the polycarbonate holes till their total cover.

#### *3.3.3.1 Characterization*

SEM images of the nanowires were obtained are presented below (Figure 3.24). In each case the diameter and the length were those of the mold of each hole. Even if the shape and structure of nanowires is quite good the density remains poor. This means that nanowires coming from many substrates must be used for the implementation of a single sensor device. Therefore, is rather impossible to follow this technique for a massive production of gas sensors. Experimentally, the best results in terms of density and homogeneity of length were those obtained in -1.05 V potential for a three-hour deposition (Figure 3.24).

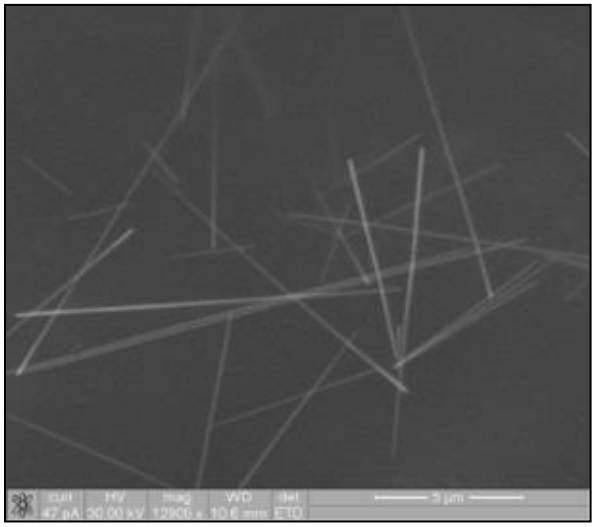

Figure 3.24: SEM image indicates the well-shaped TED nanowires.

## 3.4 Tetrapods fabrication method

A combination of thermal evaporation and controlled oxidation was used for the growth of ZnO tetrapods, inside a tubular furnace with two independent heating elements and where different gases can be fluxed (Figure 3.25). Unwanted contaminations were reduced as much as possible with the absence of catalyst or precursor. A metallic Zn foil (99.999% pure) was used as source material after a fast etching in diluted acid to remove oxide traces, which might reduce the evaporation rate. Source material was

placed in the first zone of the furnace which is labeled as “Zn evaporation zone” in Figure 3.25 and then heated up to 700 ◦C in an inert gas flow (Argon, 100 sccm). Zn vapour generated by heated source was carried by the Ar flow along the reactor up to the furnace region where it matched a 10 sccm oxygen flow (labeled “nucleation and growth zone” in Figure 3.25), which enter the reactor through a separate inlet tube. In this “matching-region”, where temperature was set in the range 600–500 ◦C, tetrapod nucleation and growth started. While floating in the gas stream, tetrapods grew until they reached the cold zone at the end of the furnace. Floating tetrapods came out of the heated zone in form of a continuous white smoke and there they deposited on the walls of reactor’s quartz tube, forming a thick and fluffy layer. The kind of thick film was grown can be easily removed from the reactor at the end of the growth procedure. In this configuration Zn source is protected from oxidation because of the presence of the inert gas, which means that the whole synthesis process can run up to complete source evaporation [46].

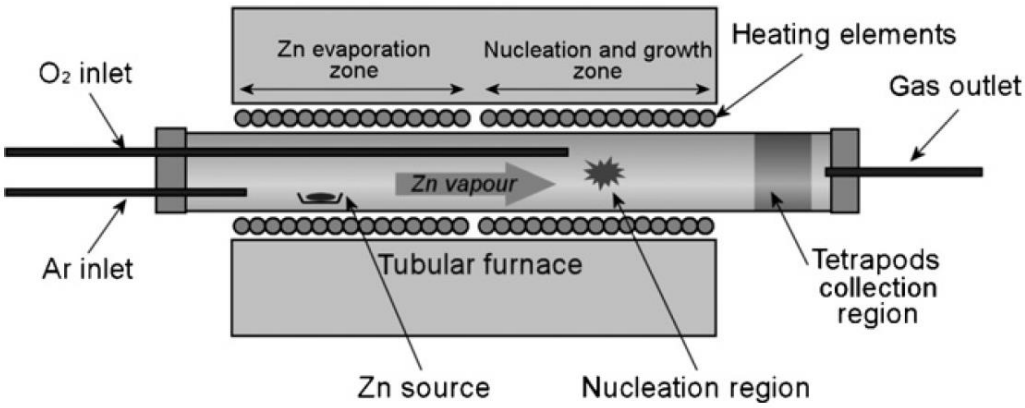


Figure 3.25: Schema of the ZnO synthesis reactor, where different positions for Zn evaporation from source material, nucleation zone and collection zone are indicated. Evaporation and nucleation temperature can be set independently. No vacuum system is used [46].

### 3.4.1 Characterization

SEM images depicted from literature [46] show that the tetrapods legs are from 50 to 200 nm thick in cross-section. The study of morphology by SEM imaging showed that the tetrapods “legs” generally are 50–200nm thick and from 2 to 4 um length (Figure 3.26). By changing the growth parameters is easy to control the dimensions of the tetrapod (Figure 3.27). Tetrapod’s thickness increases generally with higher source temperature, lower carrier gas flow and higher oxidation temperature.

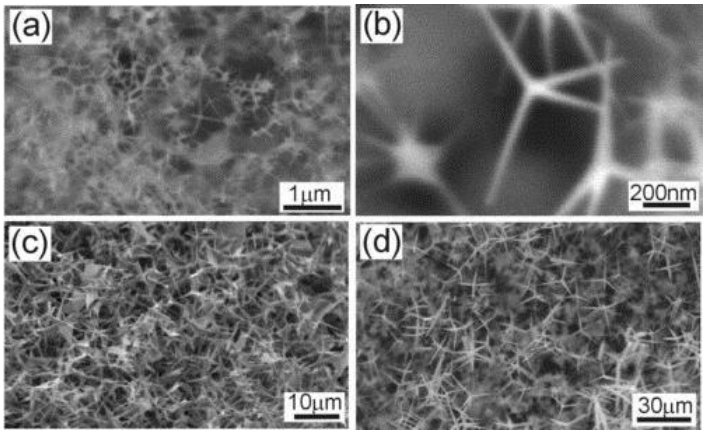


Figure 3.26: SEM image of ‘‘as-grown’’ ZnO tetrapods; (b) SEM image of the tetrapod sensing layer deposited from the isopropanol suspension; (c) a simple sensor device for testing ZnO tetrapod sensing properties: tetrapods are in the white layer between the contacts at the bottom; (d) scheme of sensor geometry: the alumina substrate is 3 by 3 mm2, the contacts below tetrapods are 200 mm spaced, the Pt heater is parallel to the sensing material at the top of the picture. (Adapted by [46]).

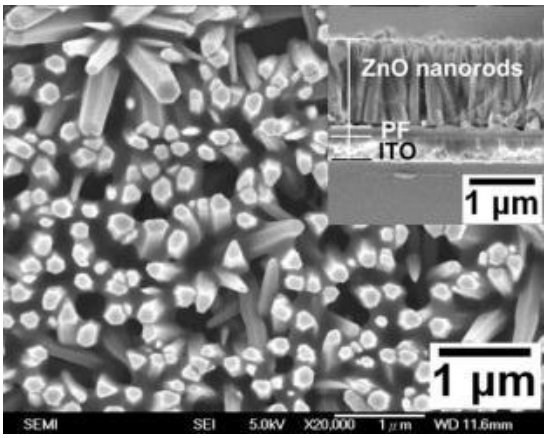


Figure 3.27: SEM images of some of the grown ZnO tetrapods with thick “legs”, obtained in different growth conditions.

For the realization of our sensors, tetrapods were deposited in the defined deposition area forming a dense tangle of nano-tetrapods that behaves as a porous film (Figure 3.28c) SEM pictures presented in Figure 3.28 show the gradual fabrication of the sensing material. It is obvious that there are many interconnections and thus many ‘‘bridges’’ between the gold contacts of the sensor as the deposition goes on.

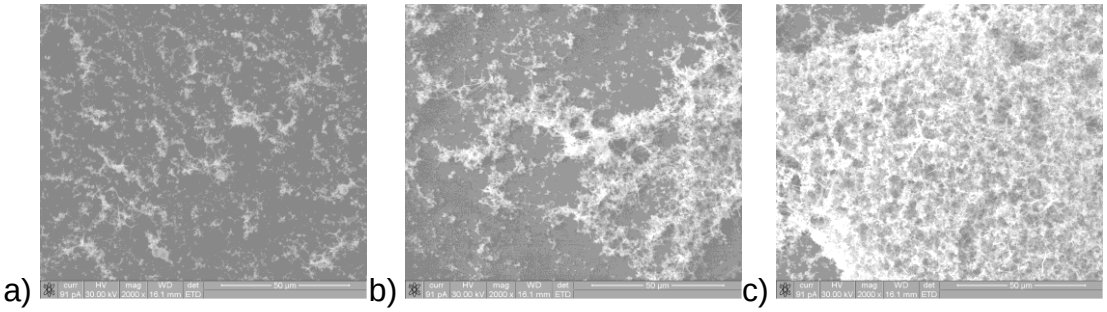


Figure 3.28: Sensors fabrication step by step based on suspension of tetrapods placed on top. a) 2mm3, b)4mm2, c)10mm2.

The sensors fabricated in this way were usable and capable to be tested in a variety of gases providing results related to several sensing properties from structural point of view (surface to volume ratio).

## 3.5 Hydrothermal growth

The hydrothermal growth is another convenient and low cost method to synthesize ZnO nanostructures which has gained immense popularity due to its simplicity and tolerable growth conditions. The hydrothermal process requires the presence of a seed material. Zinc acetate dehydrate [47] and ZnO thin film are the most common candidates. In the case of our sensors, ZnO thin films were used as seed layers.

The nucleation centers for ZnO NW growth are provided by the ZnO crystals remained on the substrate as has been already discussed. A ZnO thin film could perform the same, as it is a polycrystalline material of ZnO. Relevant studies [48] have revealed differences in the growth rate, diameter, density, and surface area of these highly oriented NW which were depended on the seed layer's physical properties and the deposition time. ZnO NWs morphology is strongly influenced by the thickness of the seed layer and the corresponding crystal size. Moreover, the surface roughness was reported to be a significant parameter determining the vertical growth of these NWs.

The alumina patterned substrate was used for the deposition of thin films. Since these ZnO NWs were grown in order to probe their properties for sensing applications, the thickness of the seed layer had to be comparable to the other tested devices; therefore 100 and 200 nm were chosen in our case.

Synthesis is carried out in aqueous solution, the growth temperatures are less than the boiling point of water. A chemical bath based on aqueous solution with 30mM Zn(NO3) and 30mM HMTA is used. The final solution is a light yellow color. The alumina patterned substrate with the deposited seed layer on top is immersed in the preheated chemical solution described above at 65 °C for a range of time between 1h and 3h depending on the desired length.

### 3.5.1 Characterization

SEM measurements have been carried out to investigate the dimension and density of ZnO growth nanowires on top of ZnO seed layers. The SEM images below (Figure 3.29 and Figure 3.30) reveal that the density of ZnO nanowires array is quite good and the

average diameter and length vary depending on the seed layer used and the applied deposition time. In case of 100nm seed layer the diameter is around 130nm and the length is 3um. On the other hand, in case of 200nm seed layer, the diameter is 100 nm and the length is 3 um. In both cases the deposition time was set in 3 hours. These results can easily be implemented in the gas sensor device.

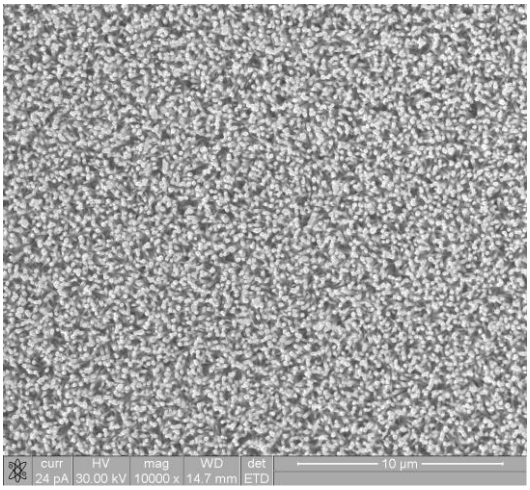


Figure 3.29: SEM images of hydrothermally grown ZnO nanowires obtained by using a ZnO seed layer of 100nm for 3 hours deposition.

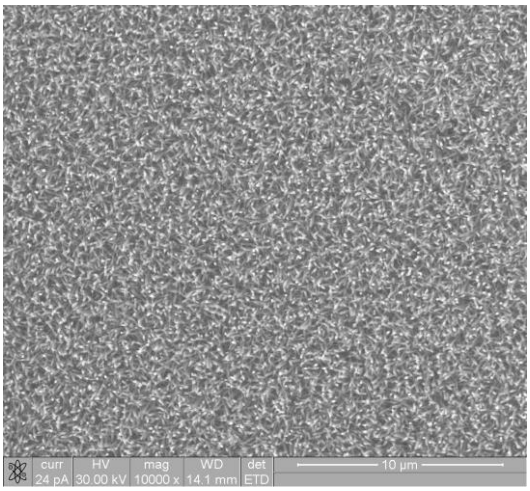


Figure 3.30: SEM images of hydrothermally grown ZnO nanowires obtained by using a ZnO seed layer of 200nm for 3 hours deposition.

## 3.6 CVD method

Chemical vapor deposition (CVD) is a chemical process used to produce high-purity, high-performance solid materials. The process is often used in the semiconductor industry to produce thin films. In typical CVD, the substrate is exposed to one or more volatile precursors, which react and/or decompose on the substrate surface to produce the desired deposit. Frequently, volatile by-products are also produced, which are removed by gas flow through the reaction chamber [49].

In our case a sapphire substrate was used for the implementation of the method. CVD is a chemical process that follows bottom-up technique as presented in Figure 3.31.

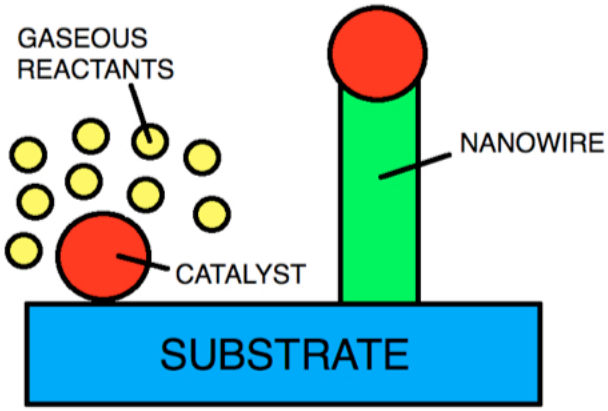


Figure 3.31: General CVD mechanism.

The details of the technique we have used have been previously reported [50]. A ZnO nanowire array on a film structure is shown in Figure 3.32. Initially the a-plane sapphire substrate is deposited with Au particles by a quick coater. The diameter of the Au particles is around 10nm (DFM image Figure 3.32a). The increasing temperature in the CVD growth force the Au particles on the a-plane sapphire substrate to coalesce together in order to form large particles, as shown in Figure 3.32. An annealing experiment is taking place to prove the formation of large Au particles at elevated temperatures. Afterwards, an a-plane sapphire deposited with the same amount of Au

was annealed at 1000 °C for 15 s with Ar gas flowed through and without Zn and O sources at a pressure of 50 mbar. The cooling process follows to reinstate the Au-deposited a-plane sapphire substrate to room temperature. The SEM image of the annealed sample is shown in Figure 3.32. After the annealing process large Au particles are formed with diameter varied from 75 nm to 25 nm. In the ZnO growth process with the Zn and O sources of this technique, the enlarged Au particles captured the Zn and O vapor to form Au–Zn alloy particles at elevated temperatures and serves as a catalyst to facilitate the ZnO nucleation. A fast growth of the ZnO nanowires and the ZnO film occurred due to the presence of a sufficient supply of Zn and O vapor sources. It is suggested that the large Au–Zn alloy particles could meet the minimum diameter requirement for the growth of nanowire in a VLS growth process [51], and supported the growth of the ZnO nanowires. Once the deposition is finished the substrate with the grown nanowires is placed into a suspension (usually isopropanol). Finally, the sonication method is applied to achieve the detachment of the nanowires from the substrate.

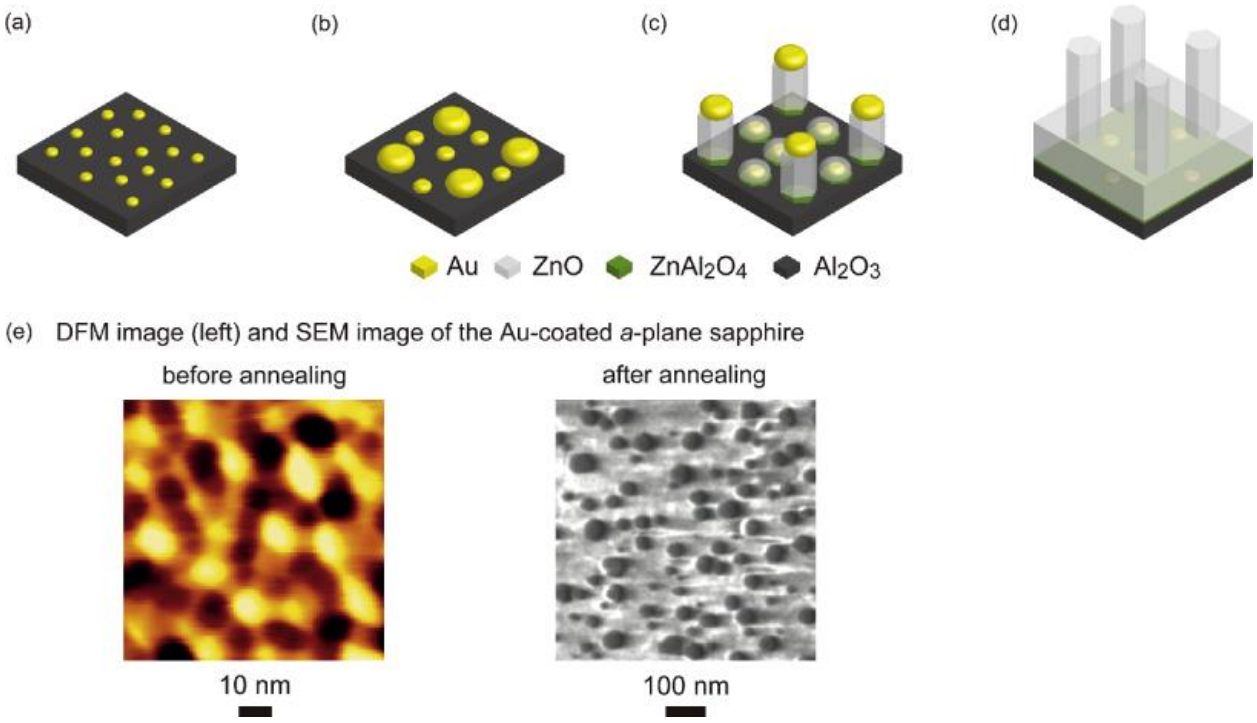


Figure 3.32: Schematic drawing of the CVD growth process of the ZnO nanowire array on a ZnO film structure on the a-plane sapphire substrate. (a) Au particles were deposited on the a-plane sapphire substrate. (b) Large Au particles were formed at elevated temperatures during the CVD process. (c) Au particles captured Zn and O vapor atoms to form the ZnO nuclei. The large droplets supported the growth of the ZnO nanowires and the small droplets supported the growth of the ZnO film. The ZnAl2O4 buffer layer was also formed at the interfaces between the ZnO and the sapphire substrate. (d) The ZnO nanowire array on a ZnO film structure was formed after the CVD growth. (Adapted by [50]).

### 3.6.1 Characterization

Morphological observations were performed by using SEM. In average nanowires length was 30um and the diameter 100nm. The density of nanowires was quite high, namely from one singe substrate is possible to retrieve all the nanowires needed for the implementation of one gas sensor. Figure 3.33 verifies the high density since they present nanowires on top of a conductive substrates coming from a couple of suspension droplets.

Nanowires length is 30 um in average and have 100nm diameter. Their density is quite high, namely is enough for the sensor's fabrication. The good results are verified by Figure 3.33 which show the dispersed nanowires on top of a conductive layer being placed by a couple of droplets.

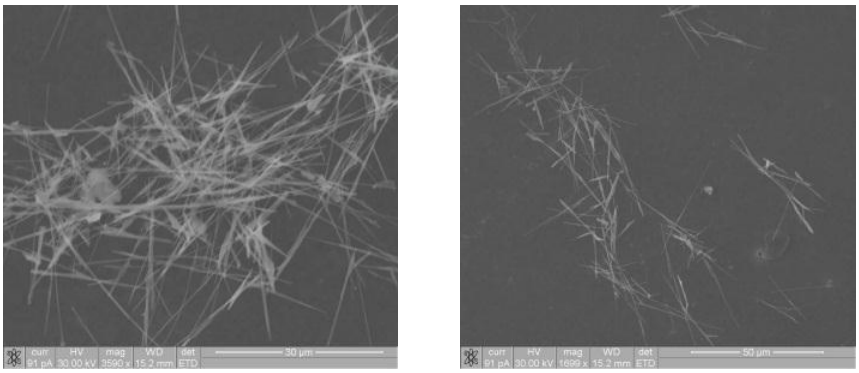

Figure 3.33: SEM images of some of the CVD nanowires dispersed on conductive layer exhibiting well formation and high density.

The final implementation of nanowires on the alumina patterned substrate (host device) is presented in Figure 3.34. The deposition zone between the two golden parts is fully covered by nanowires creating numerous of bridges between the contacts.

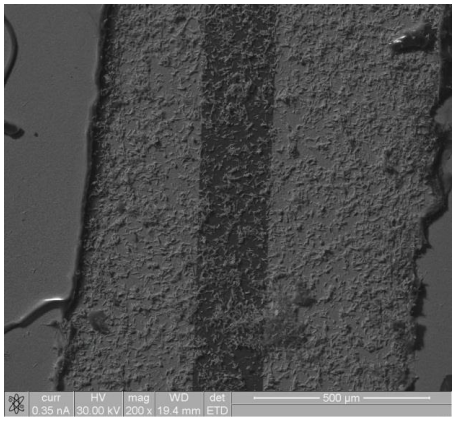

Figure 3.34: SEM images of the alumina patterned substrate host device functionalized by CVD nanowires (sensing material).

# Chapter 4 . Gas sensing's set-up and sensing mechanism.

The gas sensor setup was built at IMEM-CNR to measure the sensitivity of ZnO based nanostructures to different gases (reducing and oxidizing). Figure 4.1 shows the schematic representation of the setup.

The test system consists of three main components: the gas mixture generation system, the sensor electrical test equipment and the data acquisition system.

The gas mixture generation system can mix air with up to two different testing gases stored in cylinders. Air is divided in two lines in order to have a "dry" air line and a "100% humid" air-line. The second one is generated by bubbling dry air from the cylinder in warm water and then condensing the humidity excess at room temperature. By regulating the flows of these lines the testing mixture can be generated. The regulation is made by the flow controllers. The gas mixture then enters on one side of the test cell and exit from the opposite side.

The test cell consists of a metal box that shields the external electrical noise and helps to keep thermalized the gas around the sensor at room temperature (25°C). Inside it there are the gas sensor to be tested, a humidity sensor, a temperature sensor and a pressure sensor. All the sensors beside the gas sensor are there only to monitor the "environmental" conditions and to assure that everything works properly during the measurements. The gas sensor has four contacts, two of them for the sensing element and two for the heater. Heater is connected to a temperature controller that keeps its resistance constant at the desired temperature value. The sensing element is connected to a DC voltage generator and to an amperometer that measures the current flowing through it.

The data acquisition is performed via PC. This data acquisition system communicates with mass flow controllers and picoammeter in order to regulate and store flow values and the current data from the sensor.

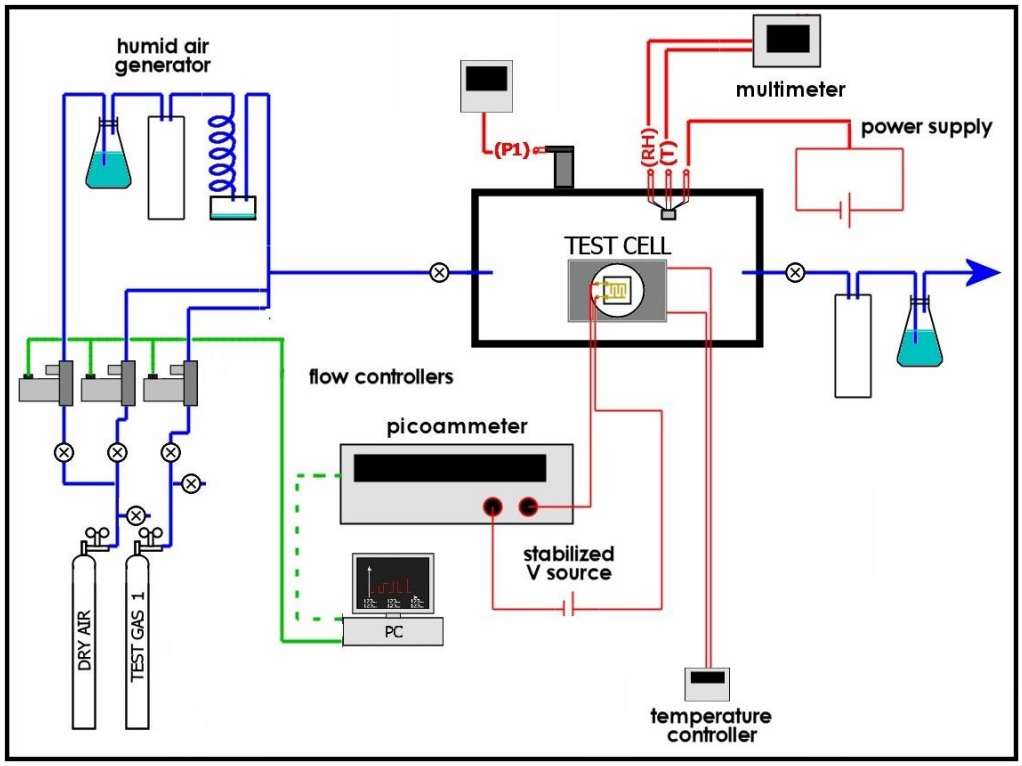


Figure 4.1: Schematic of the gas sensor set-up.

Figure 4.2 shows the real image of the sensor test setup for comparison reasons with the schematic one in Figure 4.1. The sensing gases used were commercially bought from SIAD. Nitrogen dioxide (NO2), Carbon Monoxide (CO) and Ethanol were used for our experiments.

Figure 4.2: Gas sensing set-up.

The chemo-resistive properties of the whole obtained sensors towards every gas were measured by using the flow-through technique at a constant 500 $cm^3$/ min gas flow. The DC generator which is connected to the sensing element was set at 5V for all the experiments. The change in current was monitored with respect to time through the connected Keithley 6485 amperometer, which was interfaced to the computer by a Lab-View program. The recorded data was then used to evaluate the response of the sensor to the various gases.

## 4.1 Gas sensing fundamental mechanism – State of the Art

The exact fundamental mechanisms that cause the gas response of MOS remain controversial. Nonetheless, it is generally admitted that the change in conductivity attributed to the trapping of electrons at adsorbed molecules and band bending induced by these charged molecules are responsible for a change in conductivity. Namely, MOS generally owe their conductivity to their deviation from stoichiometry. Defects such as interstitial cation or anion vacancies also play an important role in their conductivity.

There are numerous models have been proposed to describe sensing mechanism. The band bending model in Figure 4.3 and Figure 4.4 are given for the complete explanation of the mechanism. In case of oxidizing gas the negative charge trapped in the oxygen species causes an upward band bending and thus a reduced conductivity compared to the flat band situation. When O2 molecules are adsorbed on the surface of metal oxides, they would extract electrons from the conduction band and trap the electrons at the surface in the form of ions. This will lead to band bending and to an electron depleted region [52]. The electron-depleted region is so called space-charge layer, whose thickness is the length of band bending region.

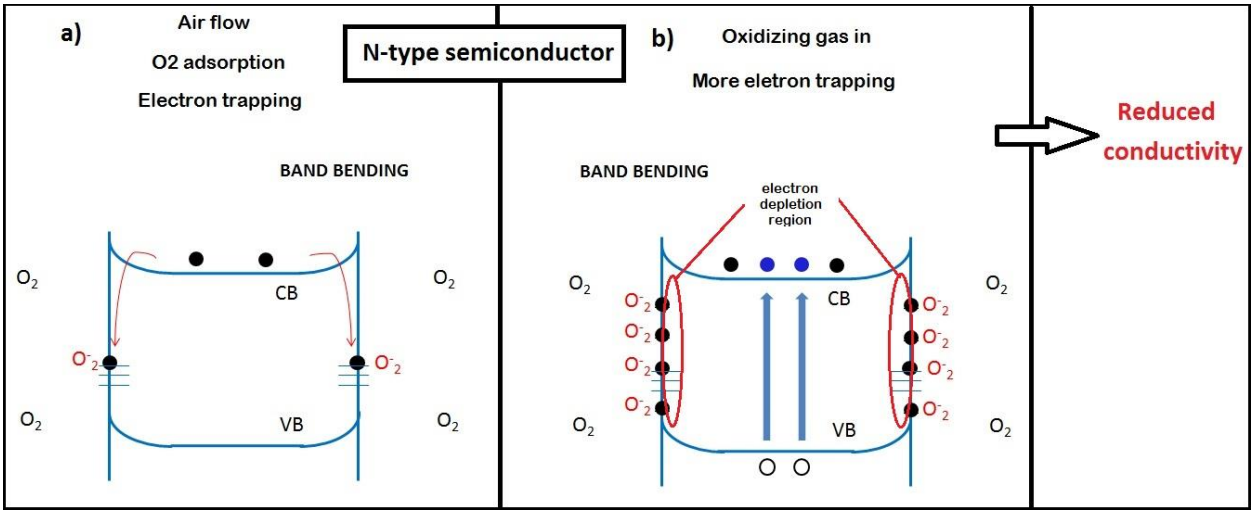


Figure 4.3: Band model of conductive mechanism upon exposure to oxidizing gas.

Reaction of the oxygen molecules with a reducing gas decreases and can reverse the band bending, resulting in an increased conductivity (Figure 4.4). The reason about this is a competitive adsorption and replacement of the adsorbed oxygen by other molecules. It is believed by several groups [52] that $O^-$ is dominant at the operating temperature of 300-400 °C which is the most investigated working temperature for most MOS.

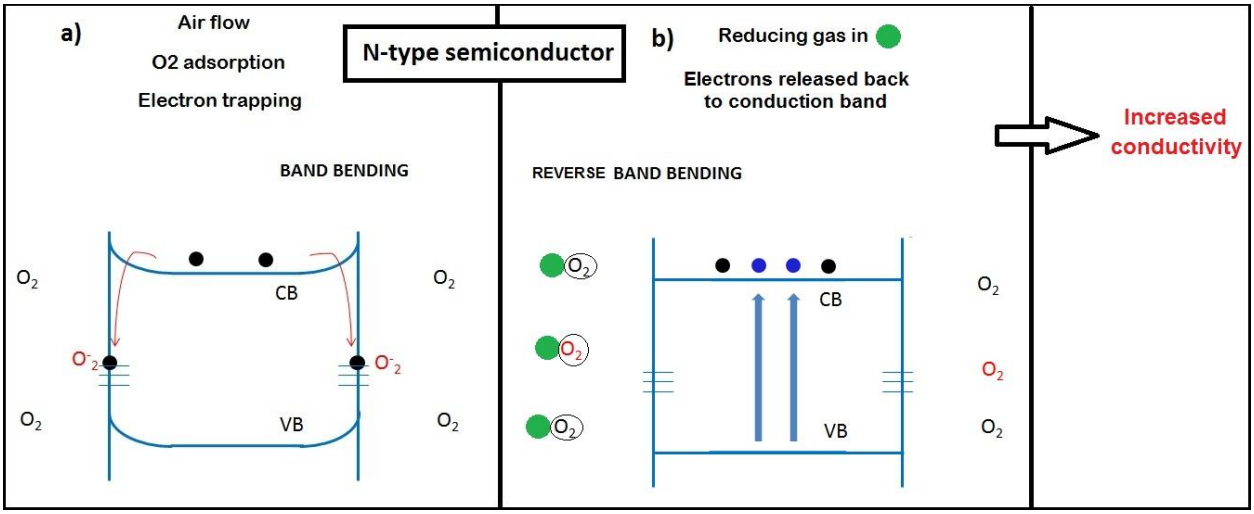


Figure 4.4: Band model of conductive mechanism upon exposure to reducing gas.

## 4.2 Design of the experiments

Analyzing the sensitivity of the ZnO based nanomaterials towards NO2, O2, Ethanol and CO is the main task in order to acquire the data needed for the assessment of the sensor's performance. Different experiments showed repeatability and reproducibility of the results. Further experiments were carried out to confirm the effects of temperature and concentration, and from the structural point of view effect of grain size and thickness was addressed. Relative humidity was set at 30% for all the experiments in order to have comparable results. The operating temperature range was from room temperature to 400°C and gas concentration varies depending on the specific analyte.

The same flow schedule in terms of time frame was used for all the measurements. In details, the sensors were allowed a stabilization time in the desired temperature of 60 min in ambient, followed by exposure to the sensing gas for 60 min which was followed by exposure to air for 60 min and continue like this till the last step which is a long stabilization time in the air.

Targeted simulations have been done in cooperation with partners in other group [53] to explain the experimental results. Their finding and evidences are presented in details in the results and discussion chapter.

# Chapter 5 . Gas sensing results and discussion

## 5.1 Grain-size and roughness effect on ethanol sensing properties of RF sputtered ZnO thin films

In this chapter, we report the grain-size and roughness effects towards improving the ethanol sensing properties of ZnO thin films deposited by RF sputtering at low gas concentration levels. Specifically, the ethanol sensing tests were performed in the 10 to 50 ppm gas concentration range under an operating temperature between 200 and 400°C. Moreover, the morphological and structural properties of the films were analyzed as a function of sputtering power at room temperature and subsequent annealing treatment. The obtained results indicate the high potential of grain-size effect as an approach to the development of high-sensitivity ZnO ethanol sensors.

As we have already discussed in the RF sputtering subchapter all ZnO thin films have wurtzite structure (see XRD patterns in Figure 5.1). Additionally, C-axis preferential growth orientation was observed for all ZnO films. Increasing sputtering power resulted in a continuous decrease of the grain size and increase of the surface to volume ratio and roughness, as it was shown in our previous work [39].

To better evidence the effect of the annealing treatment, the magnified evolution of the (002) diffraction peak is presented in Figure 5.1b. As one can see, an angle shift from 34.2 to 34.5° is observed upon annealing indicating a crystalline change which is attributed to the relaxation of the initial tensile stresses within the film while the decrease in the width at half maximum indicated an increase in crystallite size and reduction of grain boundaries [54].
However, the coupled effect of sputtering power and annealing on the grain size indicated a notable decrease only at low sputtering values, a plateau being reached above 100W [39].

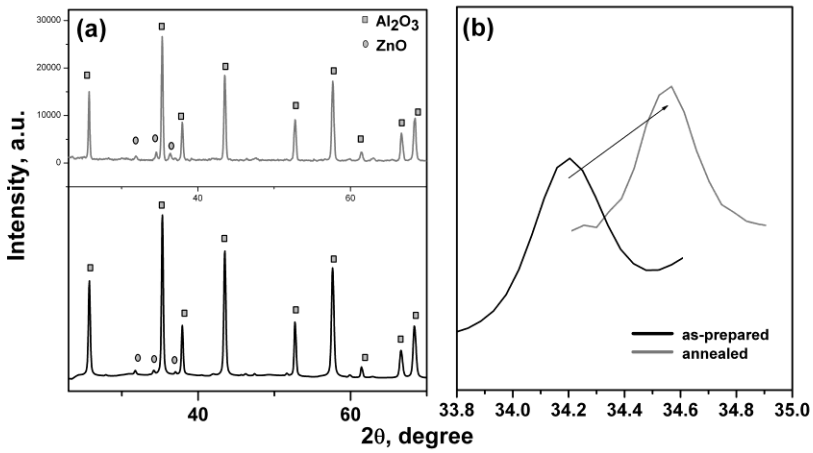


Figure 5.1: (a) XRD spectra of sputtered ZnO films before and after annealing and (b) (002) diffraction peak evolution upon annealing treatment.

The effect of the annealing treatment on the grain size was analyzed by AFM measurements as shown in Figure 5.2 depicting the morphology of 200 nm thick films of ZnO deposited at 70W, before and after the annealing procedure. The measurements confirmed the annealing treatment resulted in an increase of the grain size and roughness.

Additionally, Figure 5.3 which was created from the post processing of the AFM results reveals that the roughness changes with respect to sputtering power and annealing. In details, when low deposition rates are employed (4,1nm/min in case of 70 W sputtering power) surface roughness is about 2,5 nm, but as the deposition rate increases (8,3 nm/min in case of 150 W sputtering power) the surface becomes more rough reaching a value of about 2,95 nm. Annealing also has a crucial influence in the roughness parameter especially when is applied in a smooth surface as revealed by the big change between as-prepared and annealed sample which was fabricated in low deposition rate (case of 70W sputtering power). Specifically, the roughness is increasing from 2,95 to 5,4 nm in case of 70W sputtering power and from 2,5 to 3,6 nm in case of 150 W sputtering power.

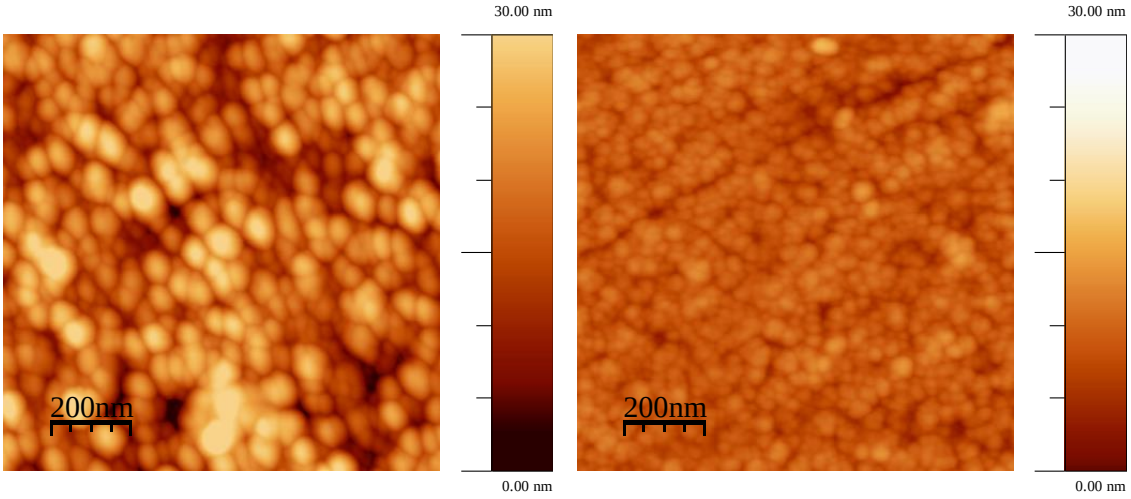


Figure 5.2: AFM images of ZnO film deposited at 70W before (left) and after annealing (right).

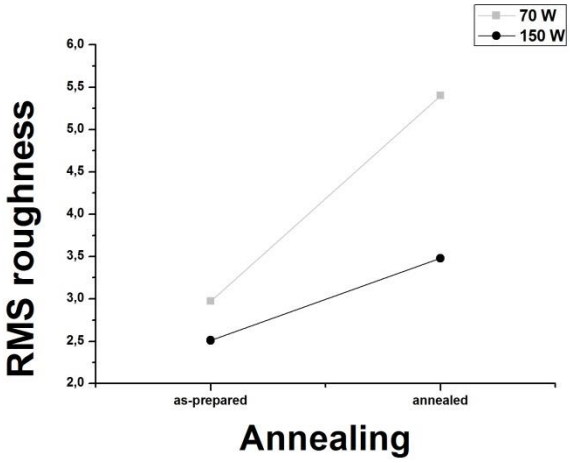


Figure 5.3: Roughness change with respect to increasing sputtering power and annealing.

Figure 5.4 shows the evolution of the grain size obtained by post-processing of the AFM images [51] with respect to the thickness of the films. It was observed that thinner films exhibited larger grains independently on the sputtering power. On the other hand, the grain size change upon annealing was almost constant with the sputtering power for all the films. It is additionally noticed that the grain size of the low power deposited thick film of 200nm was affected more than the other films by thermal annealing treatment.

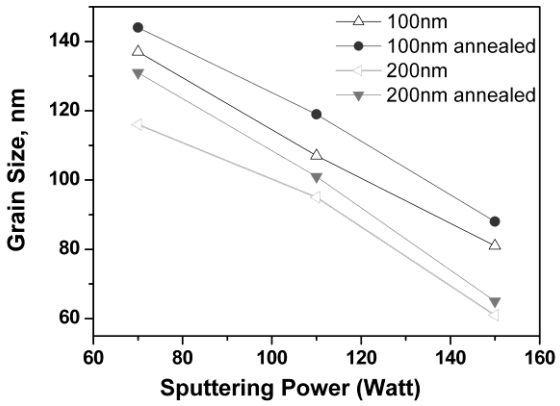


Figure 5.4: Grain size evolution with sputtering power and film thickness.

### 5.1.1 Ethanol sensing properties

Given the fact that the structural and morphological results evidenced marked grain size and roughness differences between the films deposited at low and high sputtering powers with and without subsequent annealing treatment, these films were further investigated for a better understanding of the gas sensing properties as a function of grain size and roughness. The sensor response in the presence of 50 ppm ethanol operated in a temperature range from 200°C to 400°C is depicted in Figure 5.5. It is clearly seen that the sensing response increased with the operating temperature, the highest value being recorded at 400°C independently of the sputtering power and annealing treatment. This result could be accounted to increased surface reaction for ethanol at higher temperature in accordance to several studies on the operating temperature influence on the sensitivity to alcohols and other organic vapours [55].

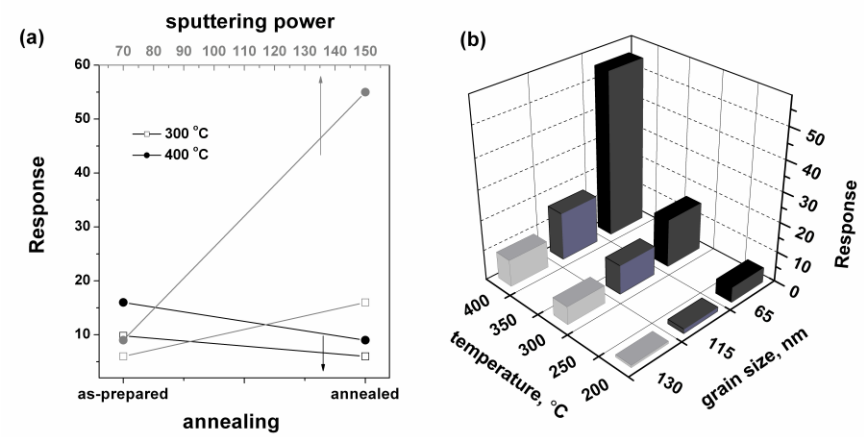


Figure 5.5: Sensor response for ZnO films to 50 ppm ethanol as a function of (a) annealing treatment of films sputtered at 70W and sputtering power of annealed films and (b) grain size and temperature.

Figure 5.5a shows that the annealing treatment of the ZnO film sputtered at 70W resulted in a decrease of the sensing response e.g. at 400°C the response decreased from 16 to 9. Considering the effect of the sputtering power and roughness on the grain size, the sensing response monitored for the annealed ZnO films previously deposited at 70W and 150W is depicted in Figure 5.5a, as well. Annealed sample of low deposition rate presents 130 nm lateral grain size and 5,45 nm roughness. As-prepared samples instead are characterized by 115 nm lateral grain size and 2,97 nm roughness. However the sensing response of the samples does not differ that much to justify the big difference in roughness value, namely it could be assumed that grain size plays a crucial role in the sensing mechanism. Further to the sensing results analysis, it should be noted that the sensing response for the film sputtered at 150W was 5-6 times higher than the one deposited at 70W. On the other hand, increasing the operating temperature from 200 to 400°C resulted in almost 10 time larger sensing response. The obtained results were further correlated to the evolution of grain size for annealed ZnO films with sputtering power depicted in Figure 5.6a. As shown in Figure 5.6b, the ZnO films with smaller grains presented higher response values, i.e. 65 nm ZnO grains exhibited 6 times higher response than 130 nm grains, reaching a value of 55 at 400°C. Given the increase in the surface area by the decrease in grain size with sputtering power, these results could be explained by the adsorption of a higher number of ethanol

gas molecules. The increased concentration of oxygen ions would result into a larger change in capacitance that indicates a higher sensor response.

Given the marked dependence of the resistance of a n-type semiconductor like ZnO film on the temperature and gas concentration, the gas sensitivity of annealed ZnO films was further monitored at 300°C and 400°C as a function of grain size (between 65 and 130nm) and chemisorbed gas concentration. As it can be observed in figure 6a, the exposure to increasing ethanol concentration resulted in an increased response. The dependence on the ethanol concentration shows two sensitivity areas indicating a difference in ethanol adsorption below and above 20ppm [56], [57]. However, on a bi-logarithmic scale (Figure 5.6b) the relationship is nearly linear, i.e. conductance change with the concentration followed a power law. Although the calculation of a precise limit of detection requires more experimental data in lower concentrations range, considering a minimum sensing response (*Response* >3), the limit of detection value extrapolated from the plot in figure 6b was observe to decrease from 1.15ppm to 0.61ppm at 400°C when grain size decreased from 115 to 65nm, while at 300°C showed little variation (from 0.84ppm decreases to 0.83ppm).

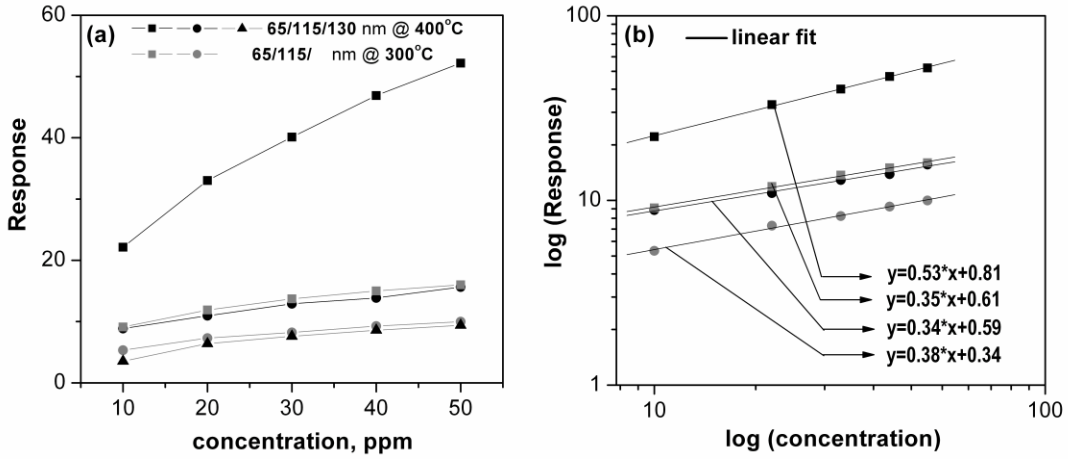


Figure 5.6: Response (a) and bi-log scale of response (b) as a function of the ethanol concentration.

The calibration curve in Figure 5.6a clearly reveals that the response generally increased with decreasing grain size. Moreover, when the grain size decreased to 65nm the magnitude of sensor response increased more and faster at the highest operating

temperature of 400°C. These results could be explained by a synergistic effect of grain size and the nature of adsorbed oxygen species on the material surface with the operating temperature, that change the electron concentration near the oxide surface and the surface conductivity, respectively. It was reported that the dominant oxygen species above 300 °C are $O^{2-}$ ones [58], that are much more unstable and energetic than $O_2$, $O_2^-$ or $O^-$ [59] and thus, they could be accounted for the increased sensitivity at higher operating temperature due to an enhanced reaction with the ethanol molecules, similarly to formaldehyde [60].

The dynamic response monitored at each tested gas concentration confirmed the temperature effect on the sensor response, as presented in Figure 5.7 that is depicting the properties of ZnO films with 65nm grains at 300 and 400°C. The plots in Figure 5.7 also indicate the sensor had a reversible response to ethanol with good recovery time at each given gas concentration that is, when exposed to a certain concentration of ethanol, the response increased rapidly and reached its equilibrium sensitivity and once ethanol was removed, the response decreased quickly to the baseline, pointing out a good reproducibility of the sensor.

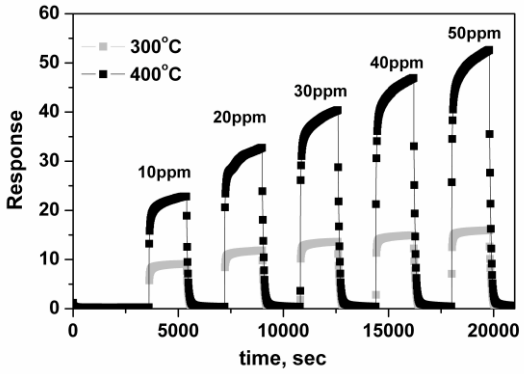


Figure 5.7: Dynamic response of the sensor with 65nm grains to 10-50ppm ethanol concentrations.

The response-recovery behaviour is a very important characteristic for assessing the performance of gas sensors. The corresponding curves plotted as a function of grain size and temperature, as depicted in Figure 5.8, confirm the different sensing properties with the operating temperature: while at 300°C a slow decreasing trend of the response

time could be observed, at 400°C a minimum is exhibited at 20ppm ethanol concentration, in agreement with previous observation. Moreover, it can be observed that the response got slower at higher operating temperature: for example, at 400°C the response to 30ppm ethanol required 138sec instead of 74 sec at 300°C for 115nm grains and 362 sec instead of 93 sec at 300°C for 65nm grains.

The response time evolution was markedly influenced also by the grain size: smaller grains exhibited the largest response time in Figure 5.8, in agreement with other reports [61]. One explanation could be related to the components of the response time as the time required for the gas molecule to diffuse to the surface and the time for the gas molecule to be adsorbed on the surface. Since the operating conditions were constant, the time for diffusion can be ignored while the time required for adsorption gets dominant. Film thickness is another parameter to consider: according to Korotcenkov and Hyodo, films thicker than 100nm respond slower than thinner ones [62], [63].

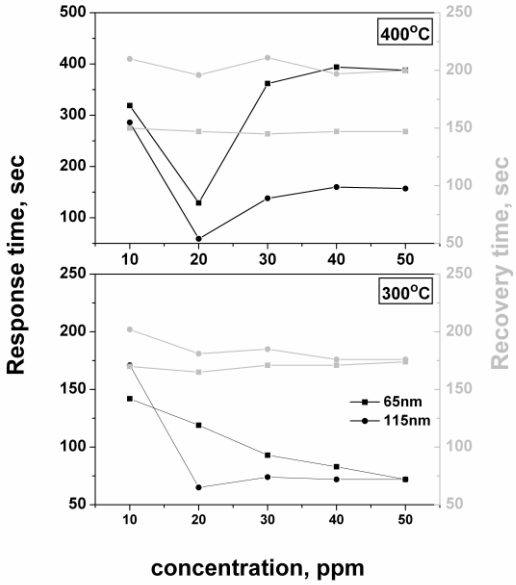


Figure 5.8: Response and recovery time evolution with grain size and operating temperature.

Opposite to the response behaviour, the recovery time evolution in Figure 5.8 showed good stability over the whole concentration range, especially for smaller grains. This is an improvement to take into account for gas-sensing applications since it is known that small grain size can lead to a loss of structural stability [64] and as a consequence to a

change of the sensing mechanism of the material [65]. Although the smaller grains appeared to respond slower to the tested gas, they recovered faster than the larger grains and the recovery change with grain size was notably higher at 400°C than at 300°C. As in the case of response behaviour, the recovery took place faster at 300°C than 400°C, i.e. the recovery from 50ppm ethanol took about 170sec at 300°C for both grain sizes, while at 400°C it required 147 sec for smaller grains and 388sec for larger ones.

Various models are presently applied to rationalize the electro-physical properties of polycrystalline materials, such as the grain-model or neck-model [66], given that the grain size and the width of the necks are the main parameters that control gas-sensing properties in metal oxides. For example, in the case of $SnO_2$ films, Bose et al. showed that both the grain and grain boundary contributed to the sensing mechanism of grains of 5 to 14 nm below 300 °C, while at higher operating temperatures (above 300 °C), the grain boundary contribution for the conductivity was dominant [67].

From the analysis of the results one can conclude that the sensing mechanism of RF sputtered ZnO films is influenced by grain size, tested gas concentration and the operating temperature. As the grain size decreases, the total surface area increases leading to an increase in sensor response. The sensitivity dependence of sputtered ZnO films on the ethanol concentration indicated a combined grain-size effect on the sensitivity from both the necks connecting the grains and the grain boundaries at operating temperature of 400°C[68]. The sharp increase with temperature indicated a synergetic effect of the grain size and temperature towards the sensitivity that could be explained by an enhanced reaction with ethanol molecules with more energetic oxygen species, dominant as $O^{2-}$ ones above 300°C [58], [69]. Since the temperature influences also the dissociation of ethanol molecules, the resulted intermediate species need to be taken into account for the reaction with adsorbed oxygen ones. However, it is necessary to point out that the relationship to grain size is dependent on the type of metal oxide, detection mechanism, and the analyzed gas.

### 5.1.2 Conclusions

The structure and morphology measurements showed the grain size of ZnO films obtained by room temperature RF sputtering decreased with the thickness and sputtering power while annealing treatment resulted in an increase of it. On the other hand, roughness was increased with both RF sputtering power and annealing. Upon exposure of ZnO films to ethanol vapors in concentration range 10-50 ppm, the ZnO film with 65 nm grains and 3,48 nm roughness exhibited higher sensitivity than the one with 130 nm grains and 5,45 roughness that was markedly increased with the operating temperature. The films with 65nm grains and 3,48 nm roughness required longer time to respond to exposure to ethanol but recovered faster than the films with larger grains. Both the response and recovery time values were below 400 sec. The results indicated that the optimization of the grain size with operating temperature is an important factor for improving the ethanol sensing properties of ZnO.

## 5.2 Investigation of surface-to-volume ratio and depletion layer impact through CO detection in advanced nanostructures.

In this chapter, CO which has one reaction with O2 (single reaction) was chosen for the investigation of surface-to-volume ratio and depletion layer impact on gas sensing. For the demand of this study two sensors have been fully measured in CO enviroment in different conditions. Sensor A was a thin-film-based ZnO nanosensor while sensor B was identical to A but with the difference that had dispersed CVD NWs on top of the film. The deposition of the film was made using a swadow mask to define the deposition area. The same shadow mask is used for the deposition of the CVD NWs as well. The schematic of the sensors is presented in Figure 5.9.

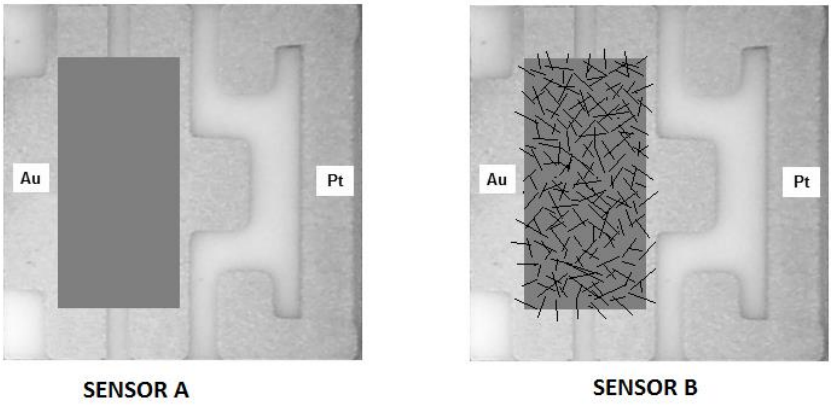


Figure 5.9: Schematic of the two obtained sensors nanostructures.

### 5.2.1. Theory: Impact of structural characteristics on sensing properties

The factors affecting the sensing properties of thin film or bulk and nanostructures are different with each other. Several sensing mechanisms along with proposed models taking into account the effect of surface-to-volume ratio and depletion layer in the ZnO-based nanostructures [70], [71], [72].

#### *5.2.1.1. Thin film and bulk*

It has been reported that sensing properties of thin films are affected by crystallite size D of the sensor materials in conjunction with the space charge depth L; to that direction three kinds of resistance-control models [70] have been proposed which assume that a sensor consists of chain of uniform crystallite of size D connected mostly with each other through necks and sometimes by grain boundaries, as shown in Figure 5.10. When D is less than 2L, the grain resistance dominates the resistance of the whole chain which dominates the sensor resistance. Thus, grains control the sensitivity. Among the three models grain control is the most sensitive condition and in turn smaller grain size would be more sensitive than larger ones as we have experimentally proved in our group's previous work (previous chapter).

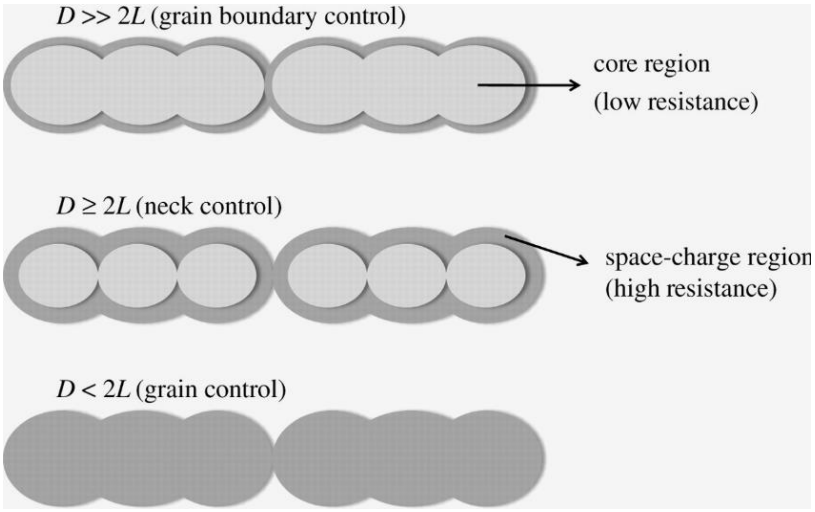


Figure 5.10: Schematic models for grain effects [71].

Additionally, a detailed formula (Eq.1) has been proposed by Niyom Hosgsith e al [72] to give the response of a sensor.

$$Rg = \frac{\Gamma t k_{gas} (O_{ads}^{ion})^{b}}{n0} X^{b} + 1$$

Where X is the target gas, b is the number of electrons, $k_{gas}(T)$ is the reaction rate coefficient, $n_0$ is the electron density of the sensor, $\Gamma_t$ is a time constant and $O_{ads}^{ion}$ is the adsorbed oxygen ions. In case of a ZnO thin film based sensors the formula can easily be applied and provide response values of the sensor.

### 5.2.2 Nanostructures

In case of nanostructures the Eq.1 cannot stand alone; two important parameters including surface-to-volume ratio and depletion layer width need to be considered in order to explain the sensing characteristics.

#### *5.2.2.1 Surface-to-volume ratio*

The surface to volume ratio is strictly related to the density of the adsorbed oxygen ions. It is rational that when the surface to volume ratio increases for the same operating conditions the density of the adsorbed oxygen ions is increasing as well. If in Eq.1 the density of the adsorbed oxygen is substituted by surface-to-volume ratio, the equation becomes:

$$(2) \quad Rg = \frac{\Gamma_t k_{gas} \left(\frac{\sigma_0 \Phi Vm}{Vs}\right)^b}{n_0} X^b + 1$$

Where $\sigma_0$ is a number of oxygen ion per unit area, $\Phi$ is a ratio of surface area per volume of material (Vm) and Vs is the system volume.

The above equation shows that response strongly depends on the surface-to-volume ratio $\Phi$. An example based on our sensors can be given to justify this statement. Sensing element of sensor A covers an area of 1,3 mm2 and 200nm thickness, while sensor B covers exactly the same area with dispersed nanowires on top as we have already mentioned. The surface-to-volume ratio can be calculated and put in Eq.3 for the sensitivity ratio as below:

$$(3) \quad \frac{R\Phi(B)-1}{R\Phi(A)-1} = \left(\frac{\Phi B}{\Phi A}\right)^b$$

$\Phi_B$ is bigger than $\Phi_A$ and this means that response of sensor B will be higher than that of sensor A.

Several studies have been made to provide experimental evidences on the surface-to-volume ratio impact on the sensor response [73]. All agree that the larger the nano-object in terms of both length and diameter the higher the response. Figure 5.11 presents an example of ethanol detection (reducing gas) which shows that even when the NWs are vertical aligned (not aligned along the conductive direction) the response is higher than that of bulk or thin film and in case of spaggeti like formation the response is enhanced even more.

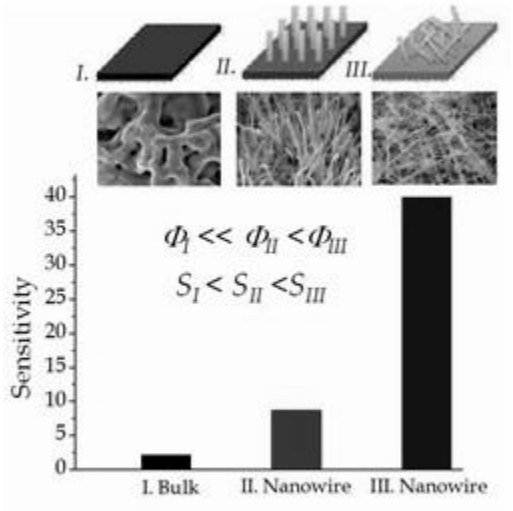


Figure 5.11: Sensor sensitivity for different ZnO sizes and morphologies with ethanol concentration of 1,000 ppm [73].

***5.2.2.2. Depletion layer***

It is important to distinguish the resistance occurring between nanowires, which is due to band bending, namely due to potential barrier between nanowires, and the resistance along the nanowires which is due to surface depletion layer and conductive channel. Several models have been proposed to describe the depletion layer in nanostructures [73], [74]. The most rational approach claims that a cylinder, which is close to the nanowire structure, is considered and a conductive channel is assumed to be along the axis of the cylinder. At an operating temperature, the oxygen ions were adsorbed by capturing an electron on the surface of the cylinder. Therefore, the depletion layer is formed on the surface of cylinder with a thickness of L, and then a size of conductive channel is reduced along the radial direction as shown in Figure 5.12a.

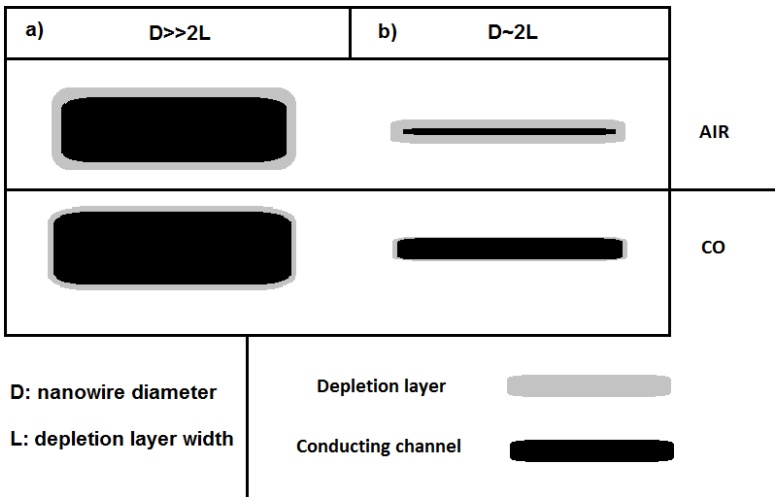


Figure 5.12: Schematic diagram of depletion layer on the surface of nanowire. a) example of much bigger diameter than depletion layer width ratio and b) diameter similar to twice depletion layer.

Based on this model the sensing mechanism can be described as follows: When the nanowire is exposed to the CO atmosphere, the CO reacts with oxygen ions on the surface and gives back electrons to ZnO sensing material resulting in increasing conductive channel, namely decreasing depletion layer.

The diameter of the nanowire plays the most crucial role in the depletion layer width in respect to the sensing properties. The categories are classified in literature in details [72]. In case of the present study nanowires diameter is in order to few nanometer which means that nanowire diameter is comparable with twice the depletion layer width. Thus, the depletion layer has strong effect make the sensor's response depend also on it. Figure 5.12b shows the impact that depletion layer has in case of our sensor expecting both the conductance and the response of the sensor to increase.

### 5.2.3 Results and discussion

#### 5.2.3.1. Structural and morphological characteristics

The SEM images of the sensor before and after CVD NWs deposition are presented in Figure 5.13a and Figure 5.13b respectively. In Figure 5.13a thin film is distinguished from the alumina strip; however alumina is still visible because of the transparency of the film. The border line between the deposition area and alumina is also visible.

In Figure 5.13b the whole area is covered by nanowires in spaghetti like formation creating extra conductive ‘’bridges’’ between the golden area and increasing the surface to volume ratio. Some extra SEM images analysis has revealed the dimensions of the nanowires which are 500nm in diameter and the length varies from 10 to 40 um.

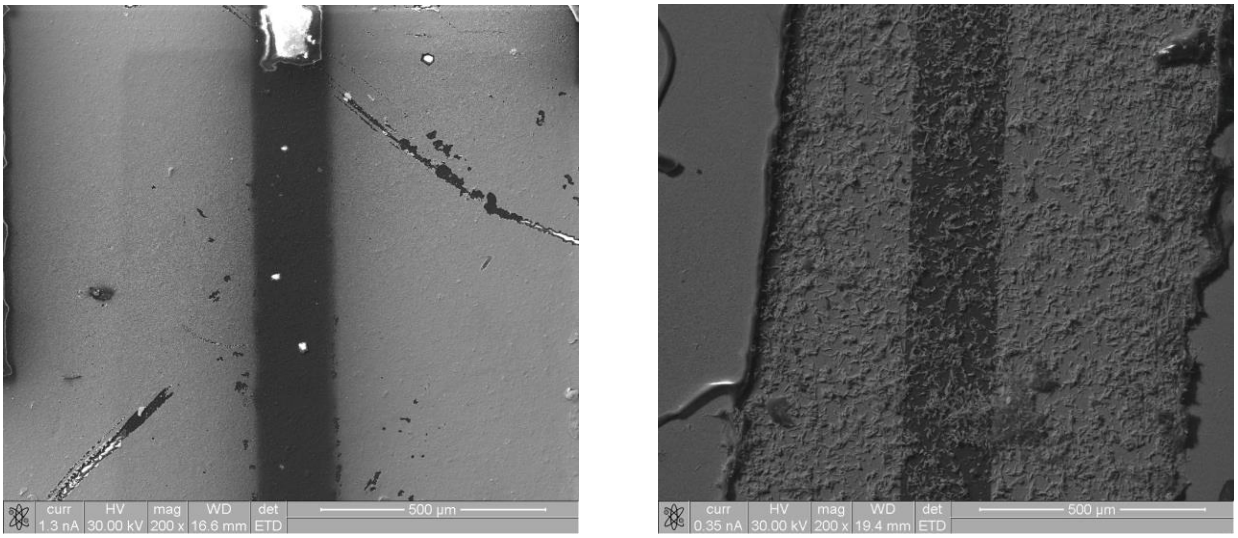


Figure 5.13: a) SEM image of ZnO thin film based sensor on alumina patterned substrate. b) SEM image of ZnO thin film based sensor on alumina patterned substrate enhanced with CVD nanowires on top.

AFM image (Figure 5.14) arises from thin film before the deposition of CVD nanowires giving information about the grain size and the roughness which are 115nm and 2,95nm respectively.

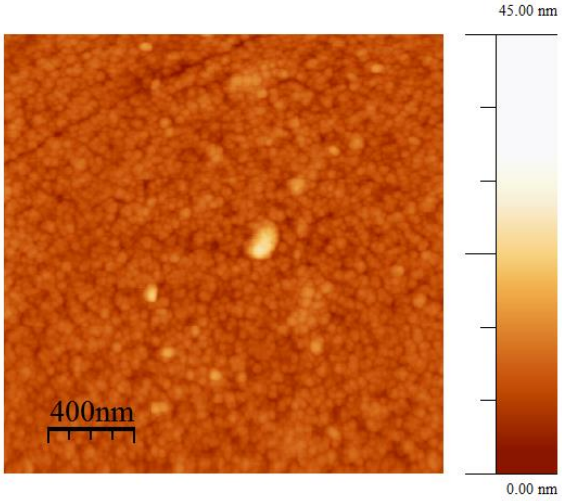


Figure 5.14: AFM image of ZnO thin film based sensor.

#### *5.2.3.2 CO sensing properties*

The present study is focused on the investigation of gas sensing differences between the two fabricated sensors considering the impact of the differences of surface-to-volume ratio and depletion layer of the active element. The high operating temperature of 400 °C is of major interest for the automotive industry and consequently is the one mainly applied in our measurements.

The calibration curve in Figure 5.15 clearly reveals that the response increased for the advanced nanostructure sensor B. These results could be explained by the combination effects of increasing surface-to-volume ratio and decreasing depletion layer width. Increasing response attributed to the surface-to-volume ratio increase as we justified before; the nanowires on top of thin film increase the surface-of the sensing element to-volume ratio. Moreover, in the case of nanowires used, their diameter of 500nm is comparable to the depletion layer width [72] indicating strong effect of the depletion layer. Thus, the depletion layer width decreases resulting in the increase of the conducting channel and therfore in the increase of the sensor sensitivity and response as well.

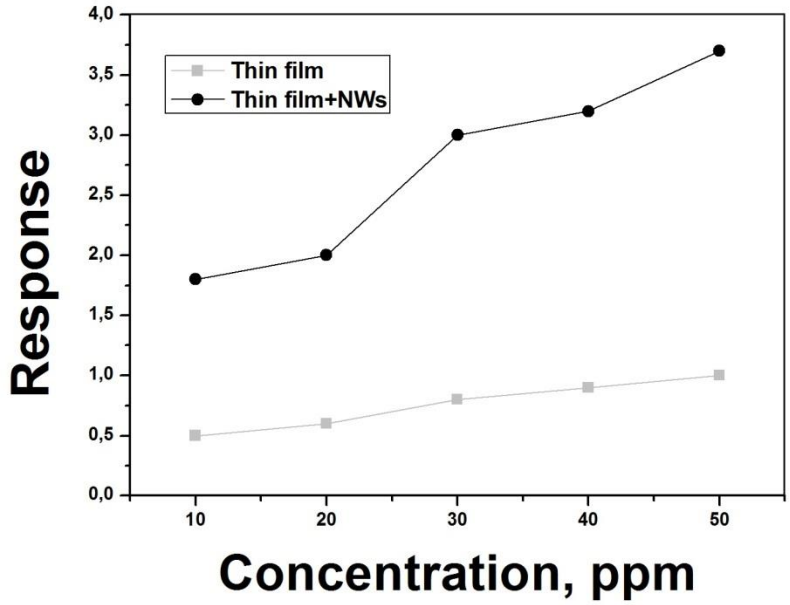


Figure 5.15: Response as a function of the CO concentration at 400°C.

The dynamic response monitored at each tested gas concentration confirmed the surface-to-volume ratio effects on the sensor response, as presented in Figure 5.16. Sensor B shows two to three times higher response than sensor A in the whole concentration range. An additional information depicted is the reversible response to CO with good recovery time at each given gas concentration. When exposed to a certain concentration of CO, the response increased rapidly and reached its equilibrium sensitivity and once CO was out, the response decreased quickly to the baseline, pointing out a good reproducibility of the sensor. Some noise is noticed in the measurements especially at 20ppm and 30ppm gas concentration that is due to undefined reasons but hardly influence the final results.

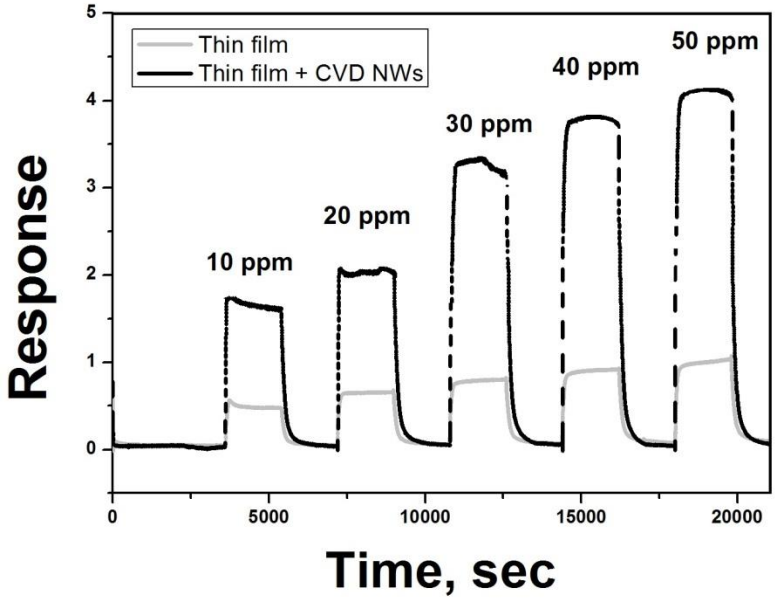


Figure 5.16: Dynamic response of the sensors in10-50 ppm CO concentration at 400°C.

The response-recovery time behavior is another sensing parameter that was assessed. The corresponding curves plotted as a function of concentration are depicted in Figure 5.17. The response and recovery behavior is quite stable over the whole concentration range for sensor B. On the other hand sensor A appears to respond slower to CO without showing a specific relationship between recovery time and gas concentration. Recovery time is similar for both sensors and always between 190 and 250 sec. which means that the speed of desorption of oxygen molecules is not depended on the kind of nanostructure. Thus, also in this testing sensing property sensor B has better performance than sensor A.

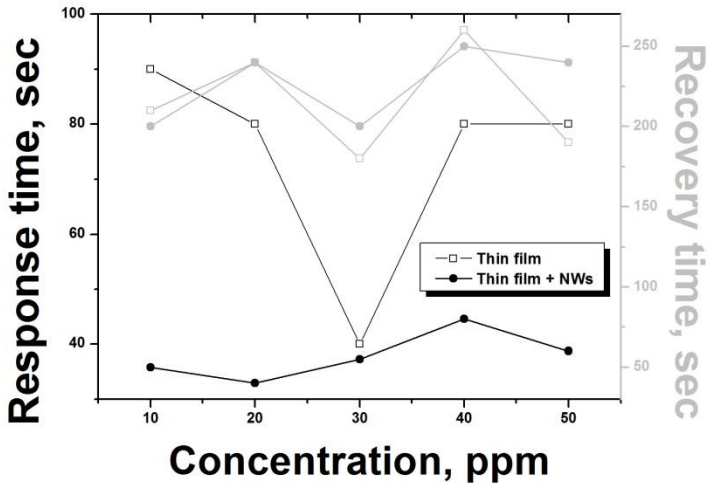


Figure 5.17: Response and recovery time evolution with concentration of CO at 400°C.

Measurements at 300°C have been performed to investigate the impact of the operating temperature in the response and sensitivity of sensor B. Figure 5.18 presents the dynamic response diagram of 50ppm which was the only concentration value that revealed a small difference between the two operating temperatures. It is clear that the impact is not high since the only observation is a small response increase of about 8% at 50ppm concentration. This means that for several applications that targeting in the detection of a much lower CO concentration this difference is rather negligible.

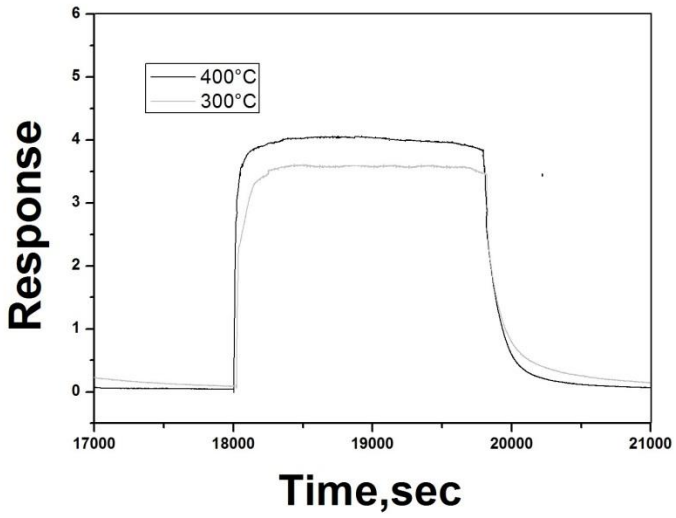


Figure 5.18: Dynamic response of the sensor as a function of operating temperature.

From the analysis of the whole results it is noticed that gas sensing mechanism is enhanced by the addition of nano-objects on top of a seed layer. Surface-to-volume ratio and depletion layer are the two parameters contributing to this fact, while operating temperature appears to play a weak role to the detection of CO when sensing material with advanced nanostructure sensors are used.

### 5.2.5 Conclusions

The measurements showed that advanced nanostructures present better sensing performance that thin films based mainly on the surface-to-volume ratio advantage and depletion layer effects. Upon exposure of ZnO film and advanced nanowires-based nanostructure to CO vapours in the concentration range 10-50 ppm, the ZnO film exhibited almost 55% lower sensitivity than the advanced nanostructure. The film required a longer time to respond, but recovery time instead was quite similar for both sensors. Last but not least, there was not observed any remarkable optimization with the increase of temperature for the advanced nanostructures.

## 5.3 Comparison between sensing properties of different ZnO-based nanostructures in Ethanol.

In this chapter, we report the growth of different nanostructures fabricated by several deposition methods and the investigation of their ethanol sensing properties. For the demand of this study three sensors have been fully measured in ethanol environment in different conditions. Sensor A is a thin-film-based ZnO nanosensor while sensor B is identical to sensor A but with the difference that had dispersed CVD NWs on top of the film. Sensor C has tetrapods on the sensing area without any seed layer beneath.

The deposition of the film and nano-objects (nanowires and tetrapods) also in this case was made using a swadow mask to define the deposition area. The schematic of the sensors is presented in Figure 5.19.

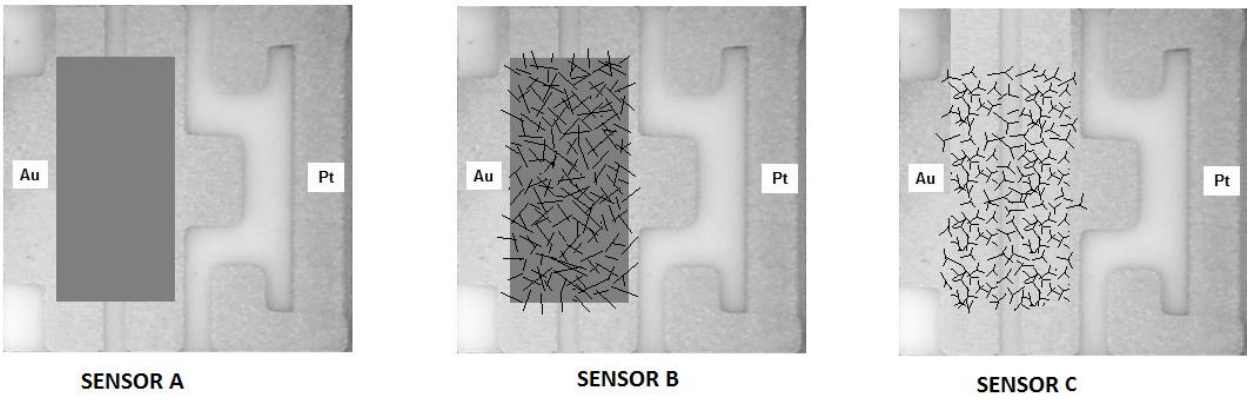


Figure 5.19: Schematic of the three obtained sensors nanostructures. Sensor A based on thin film, Sensor B based with seed layer and CVD nanowires on top, Sensor C based on tetrapods.

### 5.3.1. Structural and morphological characteristics

The XRD patterns presented previously in (Figure 5.1) hexagonal wurtzite structure for the ZnO thin film along with the diffraction peaks of alumina substrate. C-axis preferential growth orientation was observed as well [12]. The grain size of the thin film used as both sensor and seed layer was 115nm and its thickness 200nm.

The study of morphology by SEM imaging in tetrapods showed that their legs generally are 50–200nm thick (cross-section) and a few microns in length (Figure 5.22a). The nanowires were on average 20 nm in length and 200nm in diameter as appear at the SEM images in Figure 5.21. It can be also observed the presence of nanoflakes which could be attributed to the impurities during the growth process.

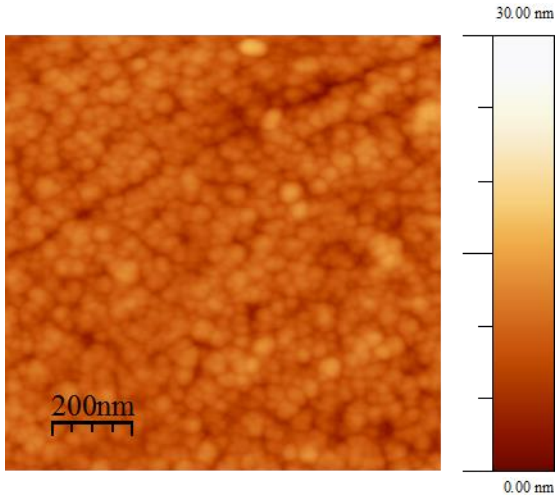


Figure 5.20: AFM image of ZnO thin film with 115nm grain size and 200nm thickness corresponds to sensor A.

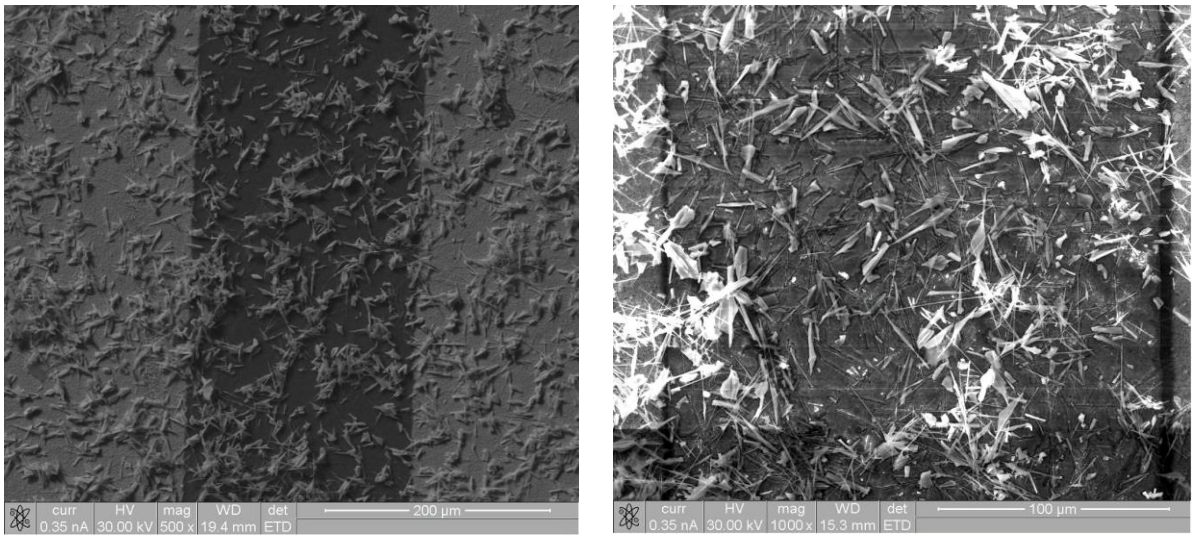


Figure 5.21: SEM images of sensor B with the grown ZnO nanowires and nanoflakes on top.

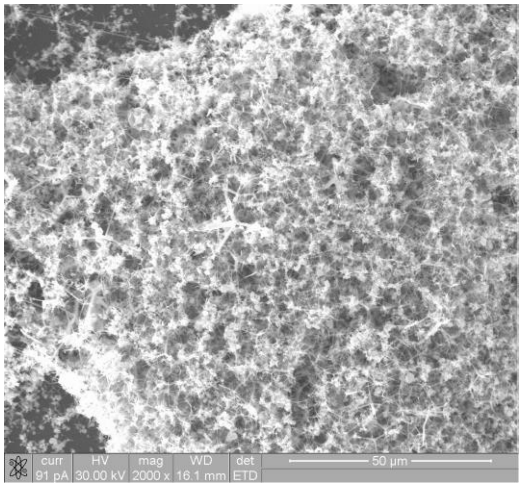


Figure 5.22: SEM image of Sensor C with grown ZnO tetrapods on top.

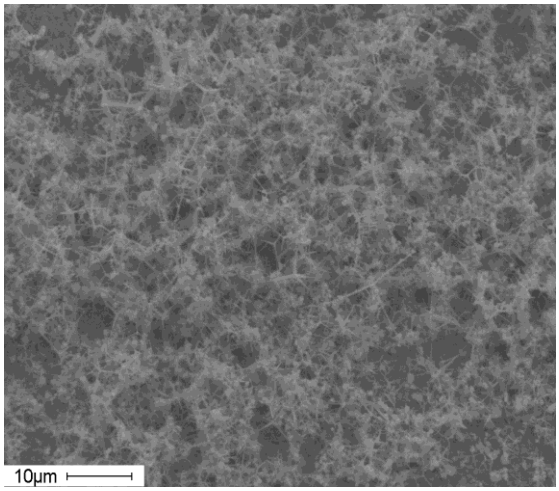


Figure 5.23: SEM image of the grown ZnO tetrapods depicted from literature for direct comparison to our tetrapod-sensor.

### 5.3.2. Ethanol sensing properties of nanostructures

The present study is focused on the investigation of sensing differences between several structures (based on ZnO) in ethanol. These series of experiments have been performed to investigate which structure could show the highest sensitivity which is of major importance for the development of a detector with high accuracy and performance.

To this direction the suspension of tetrapods and of CVD nanowires in isopropanol had to be equally concentrated. Repeatable experiments helped to approximate the minimum declination. Additionally, to avoid precipitation problems the deposition was done using continuous sonication of the suspensions. Nonetheless, tetrapods appear to mingle between each other creating a structure that seems like porous film. CVD nanowires instead create simple bridges which do not give an extra volume to the structure.

To assure that the same material in terms of quantity could be deposited in both cases, in both cases 10 mm3 of suspension placed one by one in the deposition area waiting meanwhile for the fully evaporation of isopropanol. The deposition stopped when an infinite number of contact ‘‘bridges’’ between the golden parts was observed.

The calibration curves in Figure 5.24 which present the current to time changes and response to time graph at 400°C respect to different concentration clearly reveal the difference that has been observed in previous chapter between thin film based nanostructures and their identity which is enhanced by CVD nanowires on top in terms of current flow and response. The additional information here is that the sensor with tetrapods shows current flow and response almost equal to that with TF and nanowires structure. These results could be explained by surface-to-volume ratio increase. According to SEM images surface to volume ratio is increasing more in the case of tetrapods due to tangle which observed with each other. This fact results definitely to increased sensitivity. Moreover, it seems that it is sufficient to overcome the absence of the seed layer since it acts as a porous film with spongy extensions. The current for all three sensors is increasing slowly with ethanol concentration (from 10 to 50 ppm) and the response for all sensors is more than doubled between the minimum concentration of 10 ppm and the maximum of 50 ppm. Additionally as the concentration is increasing the difference in response between sensor B and C is becoming smaller. In the lowest concentration response is 15 for sensor B and 12,5 for sensor C, while it is 35 and 34 respectively in the highest concentration.

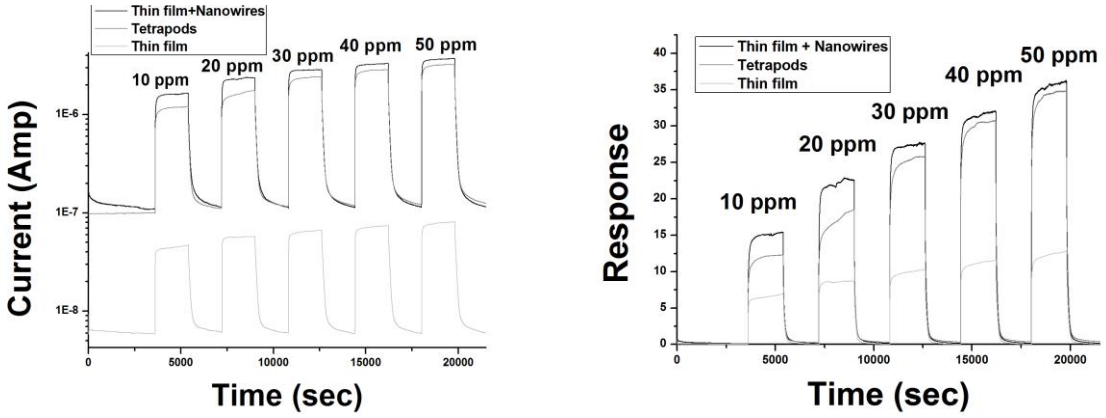


Figure 5.24: Response as a function of the ethanol concentration at 400°C and corresponded current-time diagram (from left to right).

The response-recovery behavior is the second major factor (after the sensitivity) that enhances the performance of the sensor. The corresponding curves plotted as a function of concentration, as depicted in Figure 5.25 for the advanced nanostructures of sensor B and C. The response time is decreasing with the increasing concentration for both sensors. This means that in higher concentration values the sensors based on advanced nanostructures give signal of change from the very first moments of ethanol influx. This is a characteristic that could be of major importance in the implementation of such a device. The recovery time on the other hand seems to be long enough for both sensors since it is always more than 280 sec and in case of 30 ppm concentration reaches also the 550 sec for sensor B. What is noticeable is that the behavior of these sensors does not differ that much also in case of recovery time. The possible explanation could be that the speed of desorption of oxygen molecules is not depended on the kind of nanostructure as has been already mentioned in previous chapter.

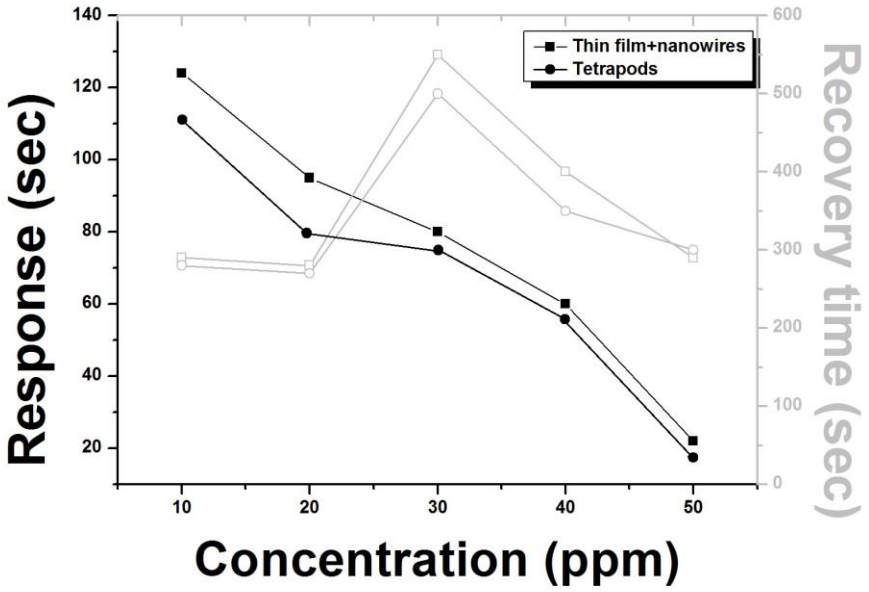


Figure 5.25: Response and recovery time evolution with concentration of ethanol at 400°C for advanced nanostructures.

### 5.3.3 Conclusions

The measurements showed that advanced nanostructures of tetrapods and thin film with nanowires on top present better sensing performance than thin films based mainly on the surface-to-volume ratio increase. Additionally, in case of sensor C the formation of a tetrapods porous film was observed, which could explain the similar sensing performance (3-5% of declination) with sensor B since the surface was rapidly increased. On the other hand tetrapods based sensor presents slightly better response and recovery time than sensor B. Moreover, the stability of sensor A should be underlined since it has been tested in several gases for many experiments with high reproducibility in time. This enhances the conclusion that sensors based on thin film are reproducible, stable and reliable.

## 5.4 NO2 gas sensing mechanism based on ZnO sensor: a combined experimental and theoretical study

In this chapter, the ZnO thin-film based sensor is used for NO2 detection; theoretical studies verify the experimental results and vice versa. Based on conductometric measurements, sensor had optimal performance at 200 °C, with detection of NO2 lower concentration of 0.1 ppm being achieved. Furthermore, ab initio simulations revealed that the sensing mechanism is driven almost exclusively by competitive adsorption between NO2 and atmospheric oxygen mediated by temperature change. The present chapter provides insights which may pave way for development and optimization of ZnO sensor for NO2 gas.

### 5.4.1. Computational details

All calculations were performed using the Quantum Espresso suite [75], which performs fully self-consistent DFT calculations to solve Kohn-Sham equation [76]. The generalized gradient approximation using Perdew, Burke and Ernzerhof (PBE) functional was employed. The core-electrons were replaced by ultra-soft pseudo potentials as described in Vanderbilt's formulation [77], and the electronic wave function (charge density) were expanded in a plane wave basis with an energy cutoff of 28 Ry

(280 Ry). The surface was modelled as a periodic slab in a supercell, and unless otherwise stated, the results presented relate 3x2 supercell. A thick vacuum layer (-15Å) was included in the direction perpendicular to the surface to ensure no interaction with its periodic images. Integration over Brillouin zone was performed using Monhorst and Pack18 with k-point sampling mesh of 4x4x1, and structures were relaxed until forces on all atoms were lower than 0.02 eV/Å. Adsorbates were symmetrically introduced on both top and bottom surfaces to avoid spurious electrostatic interactions between adjacent replicas. DFT failure to predict band gap was addressed by employing DFT+U only for the relaxed structure, with Hubbard U values of 12.0 eV on Zn 3d orbitals and 6.5 eV on oxygen 2p orbitals being used, as have been shown to work well for ZnO. Finally, spin polarization was included in calculations involving oxygen molecule.

### 5.4.2. Results and discussion

The sample exhibit a hexagonal wurtzite structure without impurity phases; it is noted that both polar and non-polar are present with non-polar facets being prominent, as shown in Figure 5.26.

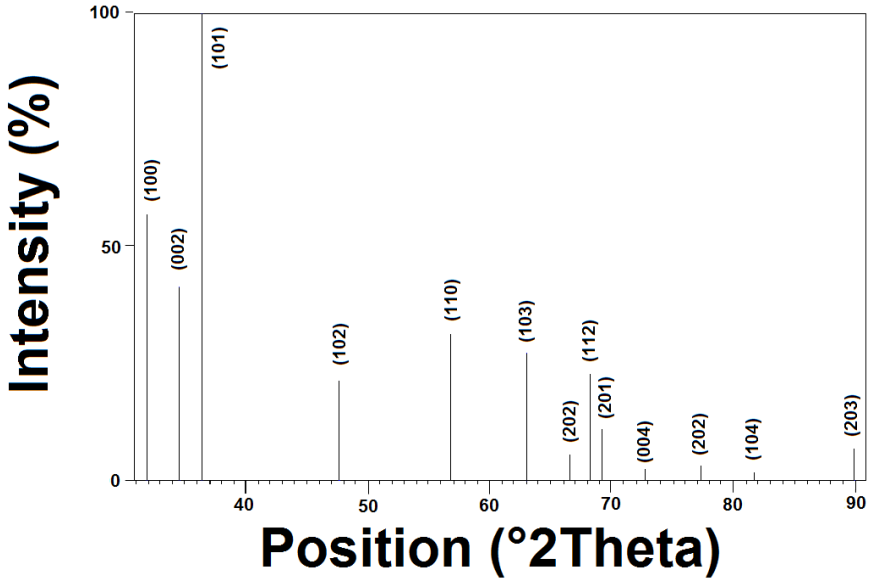


Figure 5.26: XRD spectra of sputtered ZnO film.

Conductometric measurement were performed using through technique at a constant rate of 0.5 L/min for a temperature range of 200 °C and 400 °C and heating rate of 3 K/min and at the relative humidity is kept at 30 % similar to real environment. Before the influx of gas into the chamber, the temperature within the sensor is stabilized. The procedure usually takes 1-3 hours, and it has been observed that when stabilization is achieved, the resistance of the sensing element is higher at lower temperature, with highest resistance being recorded at 300 $^{0}$ C. The explanation of this phenomenon could arise from the semiconductor conductance behavior with respect to the increasing temperature in ambient conditions. In case of ZnO, heating up the material to 200 °C follows the ionization step which increases the conductance of ZnO. At that point chemisorption is initiated and the conductance again decreases until 300-350 °C temperature when the saturation of available surface oxygen adsorption sites occurs. Therefore, the resistance is expected to be lower at 200 °C and higher at 300 °C before the infux of the gas as it is indeed (Figure 5.28).

After the influx of the gas the resistance versus time plot (Figure 5.27) shows that resistance is directly related to the concentration of NO2 and complete recovery is obtained in air. In addition, highest resistance is obtained at 200 °C for 0.5 ppm gas concentration while at 400 °C negligible changes in resistance is noted, for all gas concentration considered. Conductivity of the sensing element is temperature dependent, and it is persistent before the influx of NO2 to the chamber and complete recovery is achieved upon exposure to air, as shown in Figure 5.28. Thus, essential in unraveling NO2 gas sensing mechanism.

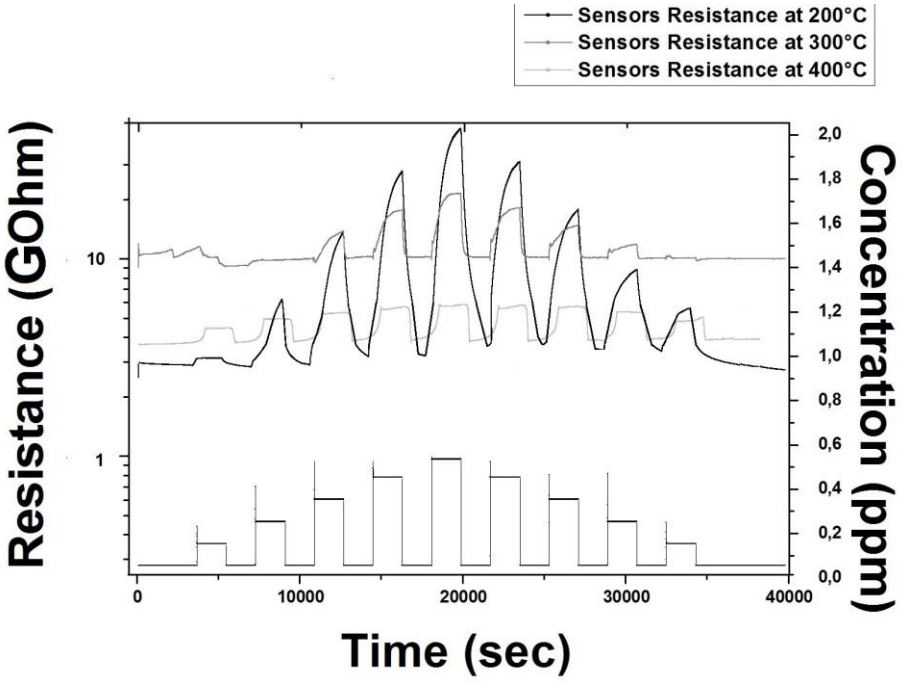


Figure 5.27: Resistance versus time for tested sensor in operating temperatures.

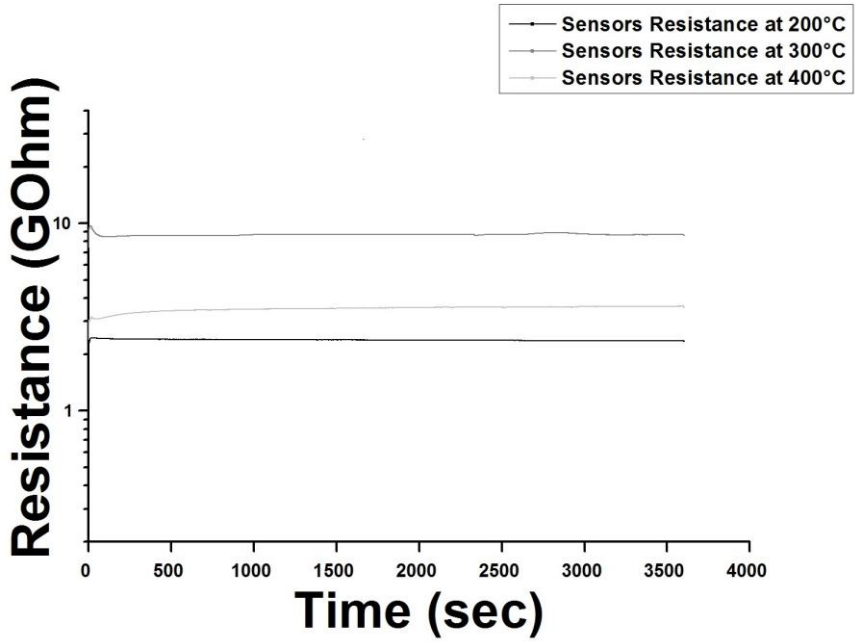


Figure 5.28: Resistance versus time for tested sensor in air and in operating temperatures.

A series of first principle calculations has been performed to assess the influence of the NO2 on the electronic properties of ZnO, and the corresponding electronic structures are presented in Figure 5.29 illustrates, it is evident that the defect-free ZnO is semiconductor, and when doped with hydrogen it becomes n-type conductor, as shown in Figure 5.29a where Fermi level shift to conduction band, consistent with experimental measurements.

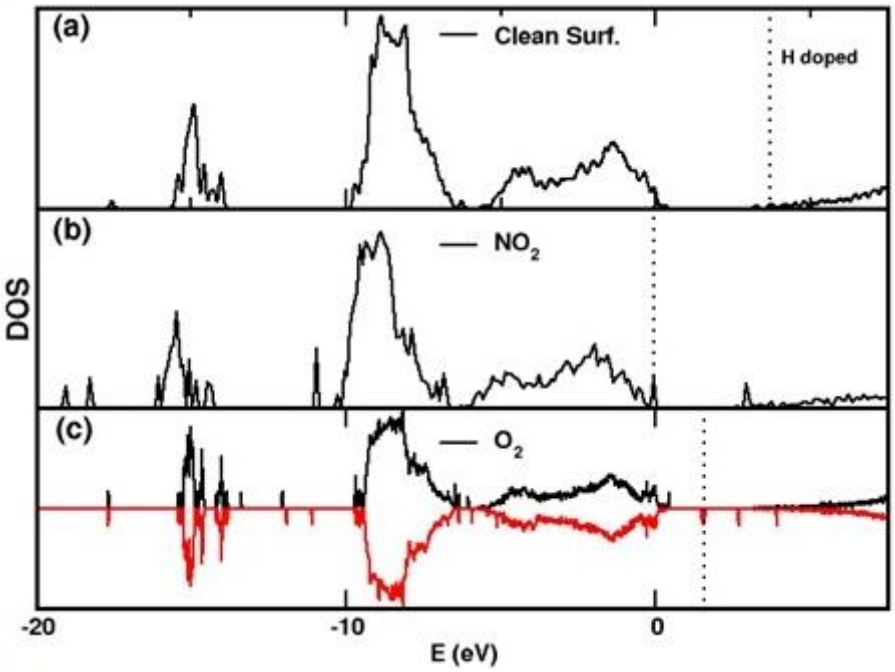


Figure 5.29: Density of State (DOS) for the (a) clean H-doped ZnO (1-100) surface, (b) Nitrogen molecule and (c) Oxygen molecule adsorbed on the H-doped ZnO (1-100) surfaces. The Fermi level is indicated by the dotted (dotted dashed line) for all systems.

Introducing NO2 in a 3x2 supercell, as shown in Figure 5.29b, the Fermi level shift back to valence band edge, signaling reduced conductivity, which is attributed to NO2 ability to trap electrons from the conduction and leads to reduced carrier concentration. The binding energy (BE) was obtained using the expression shown below:

$$BE = E_{ads+surf} - (E_{ads} + E_{surf})$$

where $E_{ads+surf}$ is the total energy of relaxed surface with adsorbate, $E_{ads}$ is the total energy of free adsorbate, and $E_{surf}$ is the total energy of the relaxed ZnO (1-100) surface. Based on binding energies, it is predicted that NO2 would bind strongly to the surface at lower temperature compared to O2.

| Adsorbate | binding energies |
|---|---|
| NO2 | -0.57 |
| O2 | -0.32 |

Table 3: Calculated binding energies for NO2 and O2 molecules, respectively.

The adsorbate was allowed to freely relax on the surface in all direction, and after the adsorption, NO2 molecule was observed to be slightly distorted, in particular, the N-O bond elongated by 0.05Å, while the bond angle contracted by 12°.

AIMD simulation of the most stable configuration of NO2 adsorption on the ZnO (1-100) surface was performed at 200 °C, 300 °C and 400 °C which correspond to temperature at sensor was operated in the experimental set-up. The evolution of the distance between the adsorbate and the closest surface atoms over the simulation time is recorded, and distant greater than that of local minimum-energy structure gives an indication as to when the adsorbate is considered to be desorbed.

As presented in Figure 5.30 at 200 °C, NO2 molecule was found to oscillate at an average distance 2.67 A above the surface atoms, an indication that the molecule is still attached to the surface. At 300 °C, the distance between adsorbate and surface remain unchanged initially, but after 2.65 ps, NO2 drift away from the surface to a distance of 3.58Å, indicating some level of desorption. While at 400 °C, NO2 is desorbed from the surface after simulation time of 0.34 ps. Thus, these results indicate that NO2 is removed from the surface at alleviated temperatures. These results are essential in unraveling the mechanism responsible for NO2 detection and the role of temperatures.

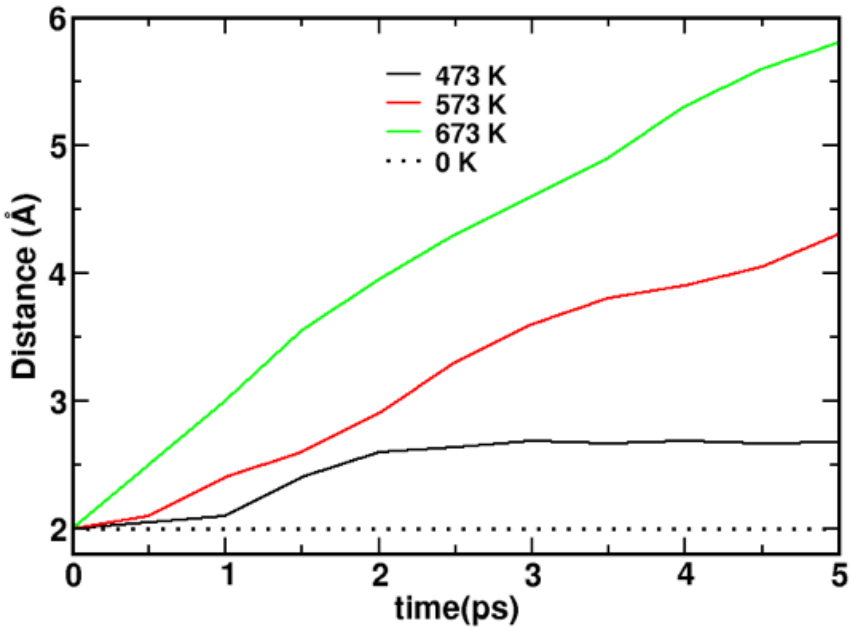


Figure 5.30: Evolution of NO2 adsorbate on the surface, the distance is taken from surface Zn atom and O atom of NO2 molecule. The variation of distance is monitored for temperature range 473-673 K.

NO2 detection is performed in oxygen rich environment, thus the role of oxygen gas in detection NO2 gas is investigated. Our calculations revealed that that oxygen molecule binds to the surface with BE which is slightly lower than that of NO2 (Table 3). Therefore, it is predicted that due to NO2 ability to binds more strongly to the surface in ambient condition, it is able to remove pre-adsorbed oxygen molecules found on the surface, which can be correlated with decreased conductivity due to NO2 ability to capture electrons from the CB, as shown in Figure 5.30. Indeed, MD calculations showed that oxygen molecule is stable on the surface up to 400 °C in particular, the molecule appears to oscillate at an average distance of 2.69Å from the surface atoms. Thus, it is anticipated that at high temperatures oxygen molecules would be re-adsorbed, replacing NO2 which tend to be unstable at high temperatures.

Response with respect to temperature and concentration presented in Figure 5.31 is in agreement with the theoretical findings since response towards NO2 appears to be higher at lower temperatures and higher concentrations. The maximum response appears in 0.1 ppm NO2 concentration at 200 °C. In 200 °C response appears to be 10 times higher than this at 300 °C and 15 times higher than this at 400 $^{0}$ C.

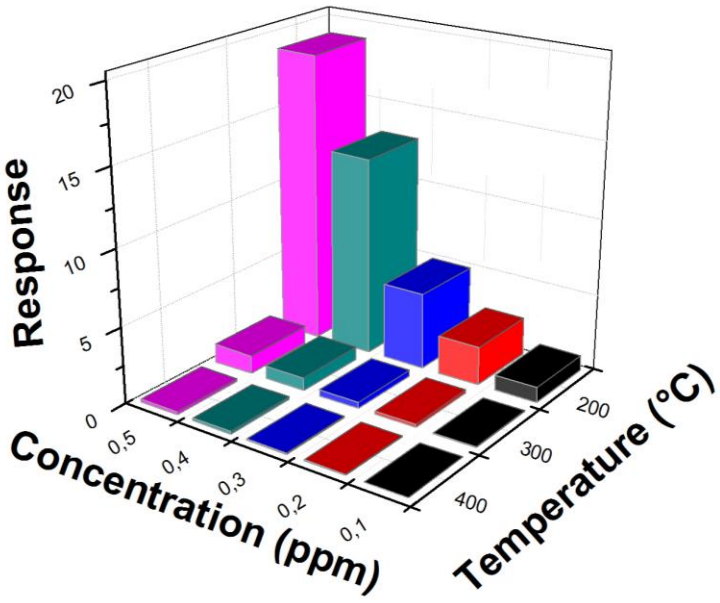


Figure 5.31: Sensors response respect to temperature and concentration.

Moreover, the sensitivity is increasing rapidly with concentration at 400 °C as presented in Figure 5.32. The sensor is quite sensitive also in the minimum tested concentration appears 500%/ppm sensitivity while presents 8800% for the maximum concentration of 0,5ppm.

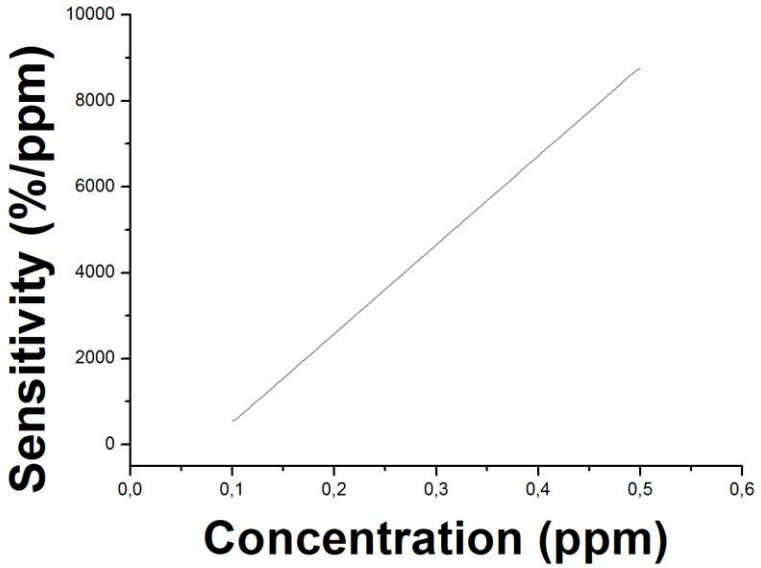


Figure 5.32: Sensors sensitivity respect to NO2 concentration at 400 $^{0}$ C.

**5.3.4 Conclusions**

Our results reveal that the sensor had optimum performance at 200 °C, in terms of sensitivity and response, with NO2 concentration as low as 0.1 ppm being detectable. Furthermore, we showed that NO2 detection is driven almost exclusively by competitive adsorption with atmospheric O2. It is observed that at elevated temperatures, NO2 undergoes molecular desorption and is replaced by oxygen molecules, which is associated by increased conductivity. Our united study gives insights on detection mechanism, which may provide crucial insights essential for improving the performance of ZnO based devices for NO2 detection and related application.

## Bibliography


[1] D. Spadaro, G. Neria, N. Donato, M. Latino, R. Passalacquaa, S. Perathonera and G. Centia C. Ampelli, "Development of Hydrogen Leak Sensors for Fuel Cell Transportation," vol. 26, pp. 333-338.

[2] Agarwal, *Anant. Foundations of Analog and Digital Electronic Circuits*.: Department of Electrical Engineering and Computer Science, Massachusetts Institute of Technology, 2005, p. 43.

[3] S. Glab and F. Ingman A. Hulanicki, "Chemical sensors: definitions and classification, Pure Applied Chemistry," vol. 63, pp. 1247-1250, 1991.

[4] Guido Faglia, Giorgio Sberveglieri Elisabetta Comini, "Electrical-Based Gas Sensing," pp. 1-61, 2009.

[5] Ya. I. Alivov, C. Liu, A. Teke, M. A. Reshchikov, S. Doğan, V. Avrutin, S.-J. Cho and H. Morkoçd Ü. Özgür, "A comprehensive review of ZnO materials and devices," 2005.

[6] Kingshuk Dutta, Amitava Pramanik Somnath Das, "Morphology control of ZnO with citrate: a time and concentration dependent mechanistic insight," vol. 15, pp. 6349-6358, 2013.

[7] Changshi Lao, Benjamin Weintraub, and Zhong Lin Wanga Sheng Xu, "Density-controlled growth of aligned ZnO nanowire arrays by seedless chemical approach on smooth surfaces," vol. 23, no. 8, 2008.

[8] Gianfranco Carotenuto, Mariano Palomba, Alessandra Mosca, Andy Horsewell, Luigi Nicolais Daniele Pullini, "In situ synthesis of high-density contact-free Ag-nanoparticles for plasmon resonance polystyrene nanocomposites," vol. 46, pp. 7905-7911, 2011.

[9] Xinyong Li, Ning Wang, Xie Quan,Yongying Chen Yuxin Wang, "Controllable synthesis of ZnO nanoflowers and their morphology-dependent photocatalytic activities," vol. 62, pp. 727–732, 2008.

[10] C. Ma, D. Moore, Y. Berta, W. Hughes and Z.L. Wang C. Ronning, "Growth mechanism of ZnS nanowires and –structures," 2004.

[11] S. Basu and S. Roy, "ZnO thin film sensors for detecting dimethyl- and trimethyl-amine vapors," vol. 15, pp. 321-326, 2004.

[12] M. Yan, X.F. Ma, H. Zhang, M. Wang and D.R. Yang X. Tang, "Gas sensing behavior of polyvinylpyrrolidone-modified ZnO nanoparticles for trimethylamine," vol. 113, no. 324–328, 2006.

[13] Eray S. Aydilb Jason B. Baxtera, "Dye-sensitized solar cells based on semiconductor morphologies with ZnO nanowires," vol. 90, pp. 607–622, 2006.

[14] Gerardo Torres-Delgado, Sergio Jiménez-Sandoval, Omar Jiménez-Sandoval, Rebeca Castanedo-Pérez Delia Cristina Altamirano-Juárez, "Low-resistivity ZnO:F:Al transparent thin films," vol. 82, pp. 35–43, 2004.

[15] Wan-Yu Wu, Jyh-Ming Ting Wen-Ting Chiou, "Growth of single crystal ZnO nanowires using sputter deposition," vol. 12, pp. 1841–1844, 2003.

[16] C Le Luyera, J Mugniera E.J Ibanga, "Zinc oxide waveguide produced by thermal oxidation of chemical bath deposited zinc sulphide thin films," vol. 80, pp. 490–495, 2003.

[17] Q. Pan, Y. Shun, Z. Tian J. Xu, "Grain size control and gas sensing properties of ZnO gas sensor," vol. 66, pp. 277-279, 2000.

[18] Z. Qian, B. Tao, G. Wang Y. Gu, "A new fiber optic sensor for detecting in situ the concentration of pharmaceuticals in blood," vol. 66, pp. 197-199.

[19] D Tarakarama Rao G.S.Trivikrama Rao, "Gas sensitivity of ZnO based thick film sensor to NH3 at room temperature," vol. 55, pp. 166–169, 1999.

[20] P.A. Atanasova, A.Ts. Andreevb, B.S. Zafirovab, E.I. Karakolevab and T.R. Stoyanchova Anna.Og. Dikovskaa, "ZnO thin film on side polished optical fiber for gas sensing applications," vol. 254, pp. 1087–1090, 2007.

[21] P.K. Basu, H. Saha, S. Basu P. Bhattacharyya, "Fast response methane sensor using nanocrystalline zinc oxide thin films," vol. 124, pp. 62-67, 2007.

[22] Bhola Nath Pal, Subhadra Chaudhuri, Dipankar Chakravorty Soumitra Kar, "One-Dimensional ZnO Nanostructure Arrays: Synthesis and Characterization," vol. 110, pp. 4605–4611, 2006.

[23] L. Vayssieres, "Growth of arrayed nanorods and nanowires of ZnO from aqueous solutions," vol. 15, pp. 464–466, 2003.

[24] A.B. Ismail, A.A. Mohamad S.S. Alias, "Effect of pH on ZnO nanoparticle properties synthesized by sol–gel centrifugation," vol. 499, pp. 231–237, 2010.

[25] Peter Gründler, "An Introduction for Scientists and Engineers," Berlin, 2007.

[26] R. Mosca, M. Zanichelli, M. Villani and A. Zappettini D. Calestani, "Aldehyde detection by ZnO tetrapod-based gas sensors," 2011.

[27] Jianjun Hanb, Yuan Zhanga, Yu"an Sunc, Bing Xiec Jiaqiang Xua, "Studies on alcohol sensing mechanism of ZnO based gas sensors Sensors and Actuators B Chemical," vol. 132, no. 1, pp. 334–339, 2008.

[28] C. Saiwan, E. Traversa T. Anukunprasert, "The development of gas sensor for carbon monoxide monitoring using nanostructure of Nb–TiO2," vol. 6, no. 3-4, pp. 359-363, 2005.

[29] Deuk Yong Lee, Young-Jei Oh Hey-Jin Lim, "Gas sensing properties of ZnO thin films prepared by microcontact printing," vol. 125, no. 2, pp. 405–410, 2006.

[30] J.Bhargava, A. Sharma, V. Vyas, G. Eranna M. Dwivedi, "CO Sensor Using ZnO Thin Film Derived by RF Magnetron Sputtering Technique," vol. 14, no. 5.

[31] M. de la L. Olvera, A. Maldonado, A. Reyes -Barranca and M. Melendez-Lira J. L. Gonzalez-Vidal, "CO sensitivity of undoped-ZnO, Cr-ZnO and Cu-ZnO thin films," vol. 52, pp. 6-10.

[32] K. Wang, Y. Li, H.T. Fang, Q.H. Lu, X.L. Ma L.H. Qian, "CO sensor based on Au-decorated SnO2 nanobelt," vol. 100, no. 1, pp. 82–84, 2006.

[33] J. P. Santos and J. A. Agapito, "The interaction of oxygen with nanocrystalline SnO2 thin films in the framework of the electron theory of adsorption," vol. 338, no. 1-2, pp. 276-280, 1999.

[34] K.L. Chopra,. New York, 1969.

[35] J.L. Vossen and W. Kern,. New York: Academic Press, 1978.

[36] John A. Thornton, "Influence of apparatus geometry and deposition conditions on the structure and topography of thick sputtered coatings," vol. 11, 1974.

[37] B.A. Movchan and A. V Demchishin, "Investigation of the structure and properties of thick vacuum-deposited films of nickel, titanium, tungsten, alumina and zirconium dioxide," pp. 653-660, 1969.

[38] Vance Bergeron, Julyan H. E. Cartwright, Rafael Escribano, John L. Finney, Hinrich Grothe, Pedro J. Gutiérrez, Jari Haapala, Werner F. Kuhs, Jan B. C. Pettersson, Stephen D. Price, C. Ignacio Sainz-Díaz, Debbie J. Stokes, Giovanni Thorsten Bartels-Rausch, "Ice structures, patterns, and processes: A view across the icefields," *REVIEWS OF MODERN PHYSICS*, vol. 84, 2012.

[39] S. Zanin, A. Pruna, D. Pullini D. Podobinski, "Effect of annealing and room temperature sputtering power on optoelectronic properties of pure and Al-doped ZnO thin films," vol. 39, pp. 1021–1027, 2013.

[40] Daniele Pullini and David Busquets Mataixc Alina Pruna, "Influence of Deposition Potential on Structure of ZnO Nanowires Synthesized in Track-Etched Membranes," vol. 159, no. 4, pp. 92-98, 2012.

[41] L. Heerman and A. Tarallo, "Theory of the chronoamperometric transient for electrochemical nucleation with diffusion-controlled growth," vol. 470, no. 1, pp. 70-76, 1999.

[42] J. M. George, P. Leisner, and L. Hultman S. Valizadeh, "Electrochemical deposition of Co nanowire arrays; quantitative consideration of concentration profiles," vol. 47, no. 6, pp. 70-76, 2001.

[43] L.D Zhangb, G.H Lib and W.Z Shena M.J Zhenga, "Fabrication and optical properties of large-scale uniform zinc oxide nanowire arrays by one-step electrochemical deposition technique," vol. 363, pp. 123–128, 2002.

[44] R. Konenkamp et al., "Thin film semiconductor deposition on free-standing ZnO," vol. 77, pp. 2575–2577, 2000.

[45] A. Pruna, S. Zanin and D. Busquets Mataix D. Pullini, "High-Efficiency Electrodeposition of Large Scale ZnO Nanorod Arrays for Thin Transparent Electrodes," vol. 159, pp. 45-51, 2012.

[46] M. Zha, R. Mosca, A. Zappettini, M.C. Carotta, V. Di Natale and L. Zanotti D. Calestani, "Sensors and Growth of ZnO tetrapods for nanostructure-based gas sensors," vol. 144, pp. 472–478, 2010.

[47] Chih-Cheng Lin and Yuan-Yao, "Synthesis of ZnO nanowires by thermal decomposition of zinc acetate dihydrate," vol. 113, no. 1, pp. 334–337, 2009.

[48] Sangwoo Lim Jaejin Song, "Effect of Seed Layer on the Growth of ZnO Nanorods," vol. 111, no. 2, pp. 596–600, 2007.

[49] S. Muller, D. Stichtenoth, D. Schwen, and C. Ronning C. Borchers, "Catalyst-Nanostructure Interaction in the Growth of 1-D ZnO Nanostructures," vol. 110, pp. 1656-1660, 2006.

[50] Yukio Sato, Mario Kurniawan, Aleksandra Apostoluk, Bruno Masenelli, Etsuo Maeda, Yuichi Ikuhara and Jean-Jacques Delaunay Miao Zhong, "ZnO dense nanowire array," vol. 23, p. 10.

[51] E.F. Wassermann K. Albert-Polaçek, "Nucleation of gold on zinc oxide," vol. 37, no. 1, pp. 65-71, 1976.

[52] Longwei Yin, Luyuan Zhang, Dong Xiang and Rui Gao Cheng xiang Wang, "Sensors Metal Oxide Gas Sensors: Sensitivity and Influencing Factors," vol. 10, pp. 2088-2106, 2010.

[53] A. Catellani, and G. Cicero K. K. Korir, "Ethanol Gas Sensing Mechanism in ZnO Nanowires: An ab Initio Study," *Journal of Physical Chemistry C*, vol. 118, pp. 24533–24537, 2014.

[54] T.H. Kim, D.Y. Kim, D.-Y. Lee, S.-O. Kim, J.-Y. Leem M.S. Kim, "Effects of annealing atmosphere and temperature on properties of ZnO thin films on porous silicon grown by plasma-assisted molecular beam epitaxy," vol. 8, pp. 123-129, 2012.

[55] S. Shao-Bo, L. Lan, Z. Xiao-Song, W. Ya-Xin, C. Xi-Ming X. Jian-Ping, "Effects of Annealing Temperature on Structural and Optical Properties of ZnO Thin Films," vol. 27, 2010.

[56] S.B. Khan, M.M. Rahman, A. Jamal, K. Akhtar, M.M. Abdullah M. Faisal, "Role of ZnO-CeO2 Nanostructures as a Photo-catalyst and Chemi-sensor," vol. 27, pp. 594–600, 2011.

[57] A. Jamal, S.B. Khan, M. Faisal M.M. Rahman, "Highly sensitive ethanol chemical sensor based on Ni-doped $SnO_2$ nanostructure materials," vol. 28, pp. 127-134, 2011.

[58] T. Chen, W. Zhang, B. Zheng, H. Shui X. Chu, "Investigation on formaldehyde gas sensor with ZnO thick film prepared through microwave heating method," vol. 142, pp. 49-54, 2009.

[59] D. Kohl, "Surface processes in the detection of reducing gases with SnO2-based devices," vol. 18, pp. 71-113, 1989.

[60] J. Zhao, J. Zheng, L. Li, Z. Zhu L. Zhang, "Hydrothermal synthesis of hierarchical nanoparticle-decorated ZnO microdisks and the structure-enhanced acetylene sensing properties at high temperatures," vol. 158, pp. 144-150, 2011.

[61] C.V. Santilli, S.H. Pulcinelli G.E. de Souza Brito, "Evolution of the fractal structure during sintering of SnO2 compacted sol-gel powder," vol. 97, pp. 217–225, 1995.

[62] G. Korotcenkov, "The role of morphology and crystallographic structure of metal oxides in response of conductometric-type gas sensors," vol. 61, pp. 1-39, 2008.

[63] N. Nishida, Y. Shimizu, M. Egashira T. Hyodo, "Preparation and gas-sensing properties of thermally stable mesoporous SnO2," vol. 83, pp. 209–215, 2002.

[64] V. Brinzari, M. Ivanov, A. Cerneavschi, J. Rodriguez, A. Cirera, et al G. Korotcenkov, "Structural stability of indium oxide films deposited by spray pyrolysis during thermal annealing," vol. 479, pp. 38-51, 2005.

[65] G.U. Kulkarni, P.J. Thomas and P.P. Edwards C.N.R. Rao, "Size-dependent chemistry: properties of nanocrystals," vol. 8, pp. 28-35, 2002.

[66] A. Rothschild, "The effect of grain size on the sensitivity of nanocrystalline metal-oxide gas sensors," vol. 95, p. 6374, 2004.

[67] P. Thangadurai and S. Ramasamy A.C. Bose, "Grain size dependent electrical studies on nanocrystalline SnO2," vol. 95, pp. 72-78, 2006.

[68] S.S. Yee, W.P. Carey X. Wang, "Transition between neck-controlled and grain-boundary-controlled sensitivity of metal-oxide gas sensors," vol. 25, pp. 454–457, 1995.

[69] Q. Wan, T.H. Wang P. Feng, "Contact-controlled sensing properties of flowerlike ZnO nanostructures," vol. 87, 2005.

[70] Jun Tamaki, Norio Miura and Noboru Yamazoe Chaonan Xu, "Grain size effects on gas sensitivity of porous SnO2-based elements," vol. 3, pp. 147–155.

[71] Y.Shimizu and M.Egashir, "Basic Aspects and challenges of semiconductor gas sensors," vol. 6, pp. 18-24, 1999.

[72] Ekasiddh Wongrat, Teerakiat Kerdcharoen, Supab Choopun Niyom Hongsith, "Sensor response formula for sensor based on ZnO nanostructures," vol. 144, pp. 67-72, 2010.

[73] Niyom Hongsith and Ekasiddh Wongrat Supab Choopun, "Metal-Oxide Nanowires for Gas Sensors".

[74] Yongki Min, "Ph.D in Properties and sensor performance of zinc oxide thin films," 2003.

[75] S. Baroni, N. Bonini, M. Calandra, R. Car, C. Cavazzoni, D. Ceresoli, P. Giannozzi, *J. Phys.: Condens. Matter*, vol. 21, p. 395502, 2009.

[76] L. Sham W. Kohn, "Self-consistent equations including exchange and correlation," *APS*, 1965.

[77] D. Vanderbilt, *Phys. Rev. B*, vol. 41, p. 7892, 1990.